Ground-based and Satellite Remote Sensing of Atmospheric Aerosols and Ultraviolet Solar Radiation

Dennis Muyimbwa

Dissertation for the degree of philosophiae doctor (PhD)

at the University of Bergen

2016

Dissertation date: April 08, 2016

Scientific Environment

A great part of this study used data which was collected under the Norwegian Programme for Development, Research and Education (NUFU), project number 33/02. Though the project ended some years back, the NILU-UV instrument which was installed in Kampala, Uganda by the NUFU project in 2005, is still working and taking measurements to date. And the Kampala NILU-UV instrument data was used in this study.

We have also received some funding from the Research Council of Norway through project 216689. The candidate was partly sponsored by the Quota scheme scholarship program from the Norwegian government through the Norwegian center for international cooperation in higher education.

To my father, John Mutto Guweddeko

Acknowledgements

I would like to thank my supervisor, Assoc. Prof. Børge Hamre and co-supervisor, Prof. Øyvind Frette, for their expert advice, support, and encouragement during my PhD study and related research. Professor Øyvind Frette, you have been like a father to me during my stay in Bergen and I thank you for the adventures and for showing me the beauty of Norway.

I am grateful to Prof. Jakob J. Stamnes for his relentless efforts towards my PhD study. I also thank Prof. Arne Dahlback from the University of Oslo for his selfless efforts towards this work.

I am sincerely grateful to the Light and Life Group; Taddeo Ssenyonga, Yi-Chun Chen, Arne Kristoffersen, Ciren Nyima, Nuozhen Gelsor, Torbjørn Taskjelle, Lu Zhao, Assoc. Prof. Svein Rune Erga, Henningsen Hanne Starfish, and Nicolausi Ssebiyonga, for the wonderful views and encouragements we shared during the weekly Wednesday meetings.

I am thankful to Makerere University for granting me a study leave to enable me finish my PhD study.

To my children; Daniella and Devlyn – thank you for allowing me time away from you to do research and write this thesis. For without you this thesis would have been completed six months earlier. To my caring, supportive, and beloved wife, Sylvia: my deepest gratitude. Your encouragement when times got tough are much appreciated and were greatly noticed.

Dennis Muyimbwa

Abstract

Satellite remote sensed data have been used to determine the aerosol climatology and to investigate the influence of the aerosol index (AI) on the ultraviolet (UV) index in coastal land areas in Serrekunda (13.28° N, 16.34° W, 17 m), The Gambia, and Dar-es-Salaam (6.8° S, 39.26° E, 24 m), Tanzania, as well as in inland areas in Kampala (0.31° N, 32.58° E, 1200 m), Uganda. Over three decades of satellite data (1979–1994 and 1996–2012) from total ozone mapping spectrometer (TOMS) and ozone monitoring instrument (OMI), which have provided measurements of backscattered radiances in the wavelength range from 331 to 380 nm, have been used. We found a high correlation coefficient between UV index and AI of 0.82 for Serrekunda, but poor correlation for Kampala and Dar-es-Salaam. The average AI for Serrekunda was found to be about three times higher than that for Kampala or Dar-es-Salaam, and a positive trend with time of the AI was found for Kampala and Dar-es-Salaam, whereas a negative trend was found for Serrekunda.

The OMI overpass UV indices were validated against the ground-based UV indices derived from NILU-UV irradiance measurements in Kampala, Uganda for the period between 2005 and 2014. It was found that the UV index values follow a seasonal pattern with maximum values in March and October. Under all-sky conditions, the OMI retrieval algorithm was found to overestimate the UV index values with a mean bias of about 28%. But under cloud/aerosol-free sky conditions, the mean bias reduced to values less than 10%. The overestimation of the UV index by the OMI retrieval algorithm was found to be mainly due to clouds and aerosols. An excessive use of old cars, which would imply a high loading of absorbing aerosols, could have been the reason for the increase with time in the AI for Kampala.

Direct solar radiances measured at a ground-based station in Bergen, Norway between February 2012 and April 2014, have been analyzed. It was found that the spectral aerosol optical thickness (AOT) and precipitable water vapor column (PWVC) retrieved from these measurements have a seasonal variation with highest values in summer and lowest values in winter. The highest value of the monthly median AOT at 440 nm of about 0.16 was measured in July and the lowest of about 0.04 was measured in December. The highest value of the monthly median PWVC of about 2.0 cm was measured in July and the lowest of about 0.4 cm was measured in December. The Ångström exponent was derived and used to deduce aerosol particle size distributions. We found that coarse-mode aerosol particles dominated most of the time during the measurement period, but fine-mode aerosol particles dominated during the winter seasons. The derived Ångström exponent values suggested that aerosols containing sea salt could have been dominating at this station during the measurement period.

In a comparison study conducted on aerosol data from AERONET (Aerosol Robotic Network) sites in Northern Norway and Svalbard, at Andenes (69.28° N, 16.01° E, 379

m) and Hornsund (77.00° N, 15.56° E, 10 m) for the period between 2008 and 2013, it was found that the five/six-year annual mean values of the AOT at 500 nm at Andenes and Hornsund were both 0.09. Less variation of the monthly mean value of the AOT at 500 nm was found at Hornsund than at Andenes. The annual mean values of the Ångström exponent of about 1.29 and 1.34 were respectively measured at Andenes and Hornsund. An Ångström exponent value of larger than 1.1 was respectively found in 68% and 84% of the observations at Andenes and Hornsund, which implies that fine-mode particles were dominating at both sites during the observation period. Despite the differences in their geographical locations with Hornsund in the arctic and Andenes in sub-arctic, both sites had a similar aerosol size distribution during summer.

List of papers

1. T. Ssenyonga, D. Muyimbwa, W. Okullo, Y. -C. Chen, Ø. Frette, B. Hamre, A. Steigen, A. Dahlback, and J. J. Stamnes, *Aerosols in coastal and inland areas in the equatorial African belt*, Appl. Opt. **53**, 2964–2973, 2014.

2. D. Muyimbwa, A. Dahlback, T. Ssenyonga, Y. -C. Chen, J. J. Stamnes, Ø. Frette, and B. Hamre, *Validation of ozone monitoring instrument ultraviolet index against ground-based UV index in Kampala, Uganda*, Appl. Opt. **54**, 8537–8545, 2015.

3. D. Muyimbwa, Ø. Frette, J. J. Stamnes, T. Ssenyonga, Y. -C. Chen, and B. Hamre, *Aerosol optical properties and precipitable water vapor column in the atmosphere of Norway*, Appl. Opt. **54**, 1505–1514, 2015.

4. Y. -C. Chen, B. Hamre, Ø. Frette, D. Muyimbwa, S. Blindheim, K. Stebel, P. Sobolewski, C. Toledano, and J. J. Stamnes, *Aerosol optical properties in Northern Norway and Svalbard*, Appl. Opt. in press, 2016.

List of Acronyms and Abbreviations

AccuRT	Accurate Radiative Transfer
AERONET	Aerosol Robotic Network
AOPs	Apparent Optical Properties
AOT	Aerosol Optical Thickness
AVHRR	Advanced Very High Resolution Radiometer
BBC	British Broadcasting Corporation
CCN	Cloud Condensation Nuclei
CFCs	Chlorofluorocarbons
CIE	Commission International de l'Éclairage
DNA	Deoxyribonucleic acid
EP-TOMS	Earth Probe Total Ozone Mapping Spectrometer
ESA	European Space Agency
FWHM	Full Width at Half Maximum
GOES	Geostationary Operational Environmental Satellite
GMS	Geostationary Meteorological Satellite
GOME	Global Ozone Monitoring Experiment
HFCs	Hydro fluorocarbons
HIRDLS	High Resolution Dynamics Limb Sounder
ICNIRP	International Commission on Non-Ionizing Radiation Protection
IOPs	Inherent Optical Properties
KNMI	Royal Netherlands Meteorological Institute
LTE	Local thermodynamic equilibrium
METEOSAT	Meteorological Satellite

MLS	Microwave Limb Sounder
NASA	National Aeronautics and Space Administration
NILU-UV	Norwegian Institute for Air Research UV
OMI	Ozone Monitoring Instrument
PAR	Photosynthetically Active Radiation
PWVC	Precipitable Water Vapour Column
RT	Radiative Transfer
RTE	Radiative Transfer Equation
TES	Tropospheric Emission Spectrometer
TOA	Top Of Atmosphere
TOC	Total Ozone Column
TOMS	Total Ozone Mapping Spectrometer
TOT	Total Optical Thickness
UN	United Nations
UNEP	United Nations Environment Programme
UTC	Universal Time Coordinated
UV	Ultraviolet
WHO	World Health Organization
WMO	World Meteorological Organization

Contents

Scientific Environment **i**

iii

Acknowledgements **v**

Abstract **vii**

List of papers **ix**

List of Acronyms and Abbreviations **xi**

1 Introduction **1**
1.1 Atmospheric Aerosols 1
1.1.1 Classification of Atmospheric Aerosols 1
1.1.2 Effects of Aerosols on Climate 5
1.1.3 Characterization of Atmospheric Aerosols 7
1.2 Solar Radiation 8
1.2.1 Ultraviolet Solar Radiation 8
1.2.2 Erythemal UV Radiation 9
1.2.3 Stratospheric Ozone Layer 11
1.3 Atmospheric Data Sampling Techniques 14
1.3.1 Ground-based Measurements 15
1.3.2 Satellite Remote Sensing 15
1.4 Objectives of this Study 17

2 Instrumentation **19**
2.1 The NILU-UV Irradiance Meter 19
2.2 The CIMEL Sun/Sky Photometers 20
2.2.1 The CIMEL CE317 Instrument 20
2.2.2 The Aerosol Robotic Network 22
2.3 Satellite Instruments 23
2.3.1 The Total Ozone Mapping Spectrometer 23
2.3.2 The Earth Probe TOMS 24
2.3.3 The Ozone Monitoring Instrument 24

3 Radiative Transfer Model **27**
3.1 AccuRT 27
3.2 Light and Matter 27
3.3 Radiative Transfer Equation 30
3.3.1 Solutions to the Radiative Transfer Equation 32
3.3.2 Classical Solution of the RTE 32
3.3.3 Solution without Scattering 33
3.3.4 Solution with Scattering and Emission 34
3.3.5 Discrete-ordinate Solution of the RTE 35

4 Introduction to Papers **37**

5 Conclusion and Outlook **41**

6 Scientific Results **45**
6.1 Aerosols in coastal and inland areas in the equatorial African belt 47
6.2 Validation of ozone monitoring instrument ultraviolet index against ground-based UV index in Kampala, Uganda 59
6.3 Aerosol optical properties and precipitable water vapor column in the atmosphere of Norway 71
6.4 Aerosol optical properties in Northern Norway and Svalbard 83

List of Figures

1.1 Dust storm billowing in Central Arizona, United States of America. Such intense dust storms (also known as haboobs in Arabic) are capable of reducing visibility to nearly zero. The picture is reprinted from [9]. . 2

1.2 Thick smoke is seen billowing from a bushfire burning near Williamtown Airport near Newcastle, New South Wales on October 17th, 2013. Photograph is reprinted from the Guardian, Australia [22]. 3

1.3 The Calbuco volcanic eruption in Southern Chile in April, 2015. Huge columns of lava and volcanic ash can be seen being sent several kilometres into the atmosphere. Reprinted from the BBC [36]. 5

1.4 A hazy atmosphere due to gaseous particles released during combustion of fossil fuels from cars. Reprinted from Nature [40]. 6

1.5 The vertical ozone profile for mid-latitude. UV radiation as a function of altitude for UV-C (red), UV-B (blue), and UV-A (green) are also shown on the graph. The width of the bar indicates the amount of energy as a function of altitude. 9

1.6 UV photons harm the DNA molecules of living organisms in different ways. In one common damage event, adjacent bases bond with each other, instead of across the ”ladder." This makes a bulge, and the distorted DNA molecule does not function properly. Reprinted from [62]. . 10

1.7 Sunburn effect or the UV index (area under the blue curve) is the product of the sunlight power spectrum (black curve) and the erythemal action spectrum or skin susceptibility to erythema (red curve) across the range of UV wavelengths [63]. The solar spectrum was calculated at a solar zenith angle of 0° using AccuRT code. 10

1.8 Solar noon erythemal UV index values derived from GOME satellite data for the year 2002; (a) yearly average, (b) yearly maximum, and (c) yearly minimum. Reprinted from the Royal Netherlands Meteorological Institute (KNMI) and the European Space Agency (ESA) [66]. . . . 12

1.9 Thin nacreous clouds made of mixtures of ice, nitric acid, and sulphuric acid form in the polar stratosphere when temperatures drop below -88 °C. In such polar stratospheric clouds, active form of chlorine are released from their reservoirs. Its beautiful colors result from the diffraction of light by ice crystals. Ozone depletion occurs in such polar stratospheric clouds. Reprinted from NASA Goddard Space Flight Center [67]. 13

1.10 Catalytic destruction of ozone by chlorine in the stratosphere. UV radiation breaks off a chlorine atom (green) from a CFC molecule. The free chlorine atom attacks and destroys an ozone molecule to form an oxygen molecule and a chlorine monoxide molecule. The chlorine monoxide molecule is attacked by a free oxygen atom to release the chlorine atom and form an oxygen molecule. The chlorine atom is then free to attack another ozone molecule and repeat the destructive process. 14
1.11 Two types of satellite orbits, geosynchronous (red) and polar orbits (yellow). Picture is reprinted from the BBC [77]. 16
1.12 Different satellite observation modes. (1) nadir (vertical), (2) limb, and (3) occultation (horizontal). Reprinted from ESA [79]. 16

2.1 The NILU-UV instruments during a field trip at Røst, northern Norway in July, 2012. The instrument is robust and can be seen being used in both wet and dry weather conditions. 19
2.2 The CIMEL sun/sky photometers (a) CIMEL CE317 portable instrument and (b) CIMEL CE318 instrument at an AERONET site at Andøya, Andenes, northern Norway. The instrument is observed in park position with the sensor head pointing nadir to avoid damage and contamination of the sensor by water, dust or snow while not in use. . . 21
2.3 The solar radiation spectrum at the top of the atmosphere (red) and at the Earth's surface (blue) calculated at a solar zenith angle of 0° using AccuRT code. The black curve represents the spectrum if the sun were to radiate as a black body at a temperature of about 5800 K (note that the values are multiplied by 6.8×10^{-5} sr, the solid angle of the solar disk). The spectrum at the surface of the Earth or at sea level, has several broken parts due to absorption by and molecules in the atmosphere. 22
2.4 A model of Aura spacecraft showing the locations of the four onboard instruments, HIRDLS, MLS, OMI, and TES. Reprinted from [87]. . . . 24
2.5 OMI measurement principle. 25

3.1 The blood Moon during total lunar eclipse. The picture is reprinted from MrEclipse.com [96]. 28
3.2 Half-range intensities in a plane-parallel atmosphere. The optical depth is measured downwards from the top to the bottom of the medium. . . . 32

5.1 The annual average TOC values inferred from OMI measurements at a site in Kampala, Uganda. 43
5.2 The annual average values of the measured UV index at local solar noon and the clear-sky UV index calculated using TOC values inferred from OMI measurements at a site in Kampala, Uganda. 43

Chapter 1

Introduction

1.1 Atmospheric Aerosols

The atmosphere is composed of molecules of gas, suspended small solid and liquid particles, known as aerosols. When these particles are sufficiently large, we notice their presence as they scatter and absorb sunlight. The scattering and absorption of sunlight by aerosols can reduce visibility (haze) and redden sunrises and sunsets. They range from fine solid particles to liquid droplets suspended in air or other gaseous environment [1]. And based on their sizes, aerosols can easily be transported far away from their sources, making their impact on climate and environmental varying from local to regional [2].

Although they are very small and highly variable, they act as condensation nuclei for cloud droplets, alter cloud optical properties, and play a role in the formation of smog and acid rain [3]. To understand their optical properties is fundamental in climate modelling and to many other applications.

1.1.1 Classification of Atmospheric Aerosols

Atmospheric aerosols are classified into two categories; natural and anthropogenic (man-made) aerosols. Natural aerosols are produced naturally from volcanoes, sea spray, sand, or wind driven erosion of surface soil. Anthropogenic aerosols are a result of human activities, such as dust from agricultural activities, smoke from burning biomass and fossil fuels, and photochemically induced smog primarily due to vehicle emissions [4, 5]. Photochemical smog is an atmospheric condition that develops when primary particles especially nitrogen oxides and combustion bi-products react in the presence of sunlight to produce hazardous secondary particles. The condition did not occur in the pre-industrial era and it is known to affect most of the major cites of the world with those with sunny, warm, and dry weather affected the most [6].

Although most of the aerosols are in the troposphere where they are removed within a few days by precipitation and interaction with Earth's surface, large volcanic eruptions can inject aerosols and trace gases much higher into the stratosphere where they may remain for a long time [7]. Aerosols are classified based on their origin, concentration, size range, structure, and chemical composition [8].

Figure 1.1: Dust storm billowing in Central Arizona, United States of America. Such intense dust storms (also known as haboobs in Arabic) are capable of reducing visibility to nearly zero. The picture is reprinted from [9].

Sea-salt Aerosols

Sea-salt aerosols are formed by evaporation of sea spray droplets from ocean surface. Particles are generated by various physical processes, especially the bursting of air bubbles entrained during whitecap formation and the tearing of droplets from wave tops [10]. The rates of particle production from both mechanisms have a strong dependence on the wind speed [11].

Sea-salt aerosols are characterized as non light absorbing, highly hygroscopic, and having coarse particle size [12]. Because of the high hygroscopy of sea-salt aerosol particles, they serve as efficient cloud condensation nuclei (CCN), altering cloud reflectivity, lifetime, and precipitation processes. Sea-salt aerosol particles are mainly constituted of sodium chloride but other chemical ions which are common in sea water, such as K^+, Mg^{2+}, Ca^{2+}, SO_4^{2-} etc, can also be found. Studies have also shown that sea-salt aerosols contain a substantial amount of organic matter [13]. The contained organic materials can change the optical properties of sea-salt as well as the hygroscopy, especially when some insoluble organic matter are present in the sea-salt particle.

The size of sea-salt aerosol ranges widely from approximately 0.05 to 10 μm in diameter, with most of masses concentrated in super-micron range (coarse-mode), and highest number concentration in sub-micron range [14]. Because of the high hydroscopy of sea-salt aerosol particles, their particle sizes may vary with humidity. They have a wide range of atmospheric lifetimes and can exist in the atmosphere for a long time. In ocean regions where wind speeds are high and other aerosol sources are weak sea-salt aerosol may be the dominant contributor to CCN [15]. Only the smallest aerosol particles with sizes from approximately 0.1 to 1 μm (e.g., those formed by bursting of bubbles at the ocean surface) are of a primary importance to large-scale atmospheric aerosol properties [7].

Dust Aerosols

Dust originates from land surfaces and it is composed of solid particles. Dust particles if they are sufficiently many as shown in Fig. 1.1, are capable of reducing visibility

to nearly zero and can posse health implications. Dust aerosol particles can scatter and absorb solar radiation, act as CCN, and as a source of nutrients to ecosystems [16, 17]. Studies have shown that dust aerosols blown from the Sahara desert is the main source of minerals that fertilize the Amazon basin [18, 19]. The sizes of dust particle are important as they influence most of the interactions of dust with climate and also determines the atmospheric lifetime and transport of dust aerosols [20]. Most of the dust particles (e.g., composed of silicon) are not soluble in water. Therefore, dramatic changes of aerosol particle shape and structure in the humidity field are rare events as compared to sea-salt aerosols. However, the mineral core may still be covered by a water or ice shell in high humidity conditions and this can modify the optical properties of the aerosol particles [7].

Secondary Aerosols

Secondary aerosols are formed in the atmosphere by gas-to-particle conversion processes such as nucleation, condensation, and heterogeneous and multiphase chemical reactions [21]. These aerosol particles are composed of mainly sulphates and nitrates. Also various organic substances (originating e.g., from gases emitted by plants) can make a large contribution in the total aerosol mass. For example, inorganic gases such as sulphur dioxide, nitrogen dioxide, and ammonia are converted into particulate phase sulphates, nitrates, and ammonium. In particular, sulphur dioxide is oxidized to sulphuric acid and the of conversion is influenced by the presence of heavy metal ions (e.g., iron, manganese, etc) [7]. Also atmospheric oxidation of volatile organic compounds can convert gases to particulate matter [21].

Figure 1.2: Thick smoke is seen billowing from a bushfire burning near Williamtown Airport near Newcastle, New South Wales on October 17th, 2013. Photograph is reprinted from the Guardian, Australia [22].

Biological Aerosols

Biological particles are suspended in the atmosphere in form of pollens, fungal spores, bacteria, viruses, insects, fragments of plants and animals, etc. Their volumetric concentration depends on the season, location, and height of the sampling volume with

smallest values at higher altitudes and in winter time (e.g., at higher latitudes). Bio-aerosols may act as major contributors to CCN for regions where other aerosols sources are weak e.g., in pristine regions like the Amazon basin [23–25]. Suspended biological particles are a major vector for animal, plant, and human diseases [8], and have been found to enhance allergies, asthma, and other respiratory conditions [26, 27].

Bio-aerosols are characterized by the extreme particle size range and enormous heterogeneity [28]. Bacteria, for example has an internal structure and cannot be considered as an homogeneous object in light scattering studies. Bio-aerosols can occupy up to 30% of the total aerosol volume at a given location especially in remote continental areas [7]. The concentration of bio-aerosols is at least three times smaller in remote marine environments. But bio-aerosols produced inland can also travel very long distances owing to their low densities. Bio-aerosols (e.g., bacteria and viruses) can be attached to other particles (e.g., dust, pollen, spores) and travel large distances using other particles, including cloud droplets, as a means of transport [7].

Smoke Aerosols

Smoke aerosols originate from forest, grass, and other types of fires (see also Fig. 1.2). Smoke from bush fires constitutes about 5% to 10% of black carbon with organic carbon accounting for much of the particle mass [29]. Landscape fires produce about 60 million tons of smoke per year [30]. This is equivalent to about 30% of the global total mass of black and organic carbon emitted annually [31]. This is a small number compared to other aerosol sources but has important local effects. Smoke aerosols can lead to health complications in humans, animals, and plants, reduce visibility, and affect the atmospheric heat balance due to generally large values of light absorption by soot as compared to other aerosol sources [7].

Studies have shown that aerosols transported to the Arctic from highly polluted areas in Europe can lead to a decrease in the planetary albedo [32]. This is due to atmospheric absorption effects of soot and also due to increased absorption of polluted snow and ice. Soot can alter the properties of clouds by affecting cloud reflectivity and lifetime and thus affecting precipitation [33, 34].

Smoke can reduce surface UV-B irradiance by over 50% near fire sources but the net reduction in global UV-B irradiances can be about 10% larger than the reduction in global UV-A irradiances [35]. Smoke aerosols contain large amount of soot and soot particles consist of aggregates with sizes greater than 1 μm with many particles of a smaller size as well [7].

Volcanic Aerosols

Volcanic eruptions are capable of ejecting enormous amount of primary particles and gases (e.g., gaseous sulphur) very high into the atmosphere. Most of the particles ejected from volcanoes (dust and ash) are water insoluble mineral particles, silicates, metallic oxides such as SiO_2, Al_2O_3 and Fe_2O_3, which may remain in the atmosphere for a long time [7]. Figure 1.3 shows a volcanic eruption of mountain Calbuco in Chile in April 2015, and huge amounts of volcanic ash are observed being ejected high into the atmosphere. Volcanic aerosols are capable of remaining in the atmosphere for a long time.

Figure 1.3: The Calbuco volcanic eruption in Southern Chile in April, 2015. Huge columns of lava and volcanic ash can be seen being sent several kilometres into the atmosphere. Reprinted from the BBC [36].

Volcanic aerosols in the troposphere have important effects on the Earth's climate, both directly through absorption and backscattering of solar radiation, and indirectly through modification of clouds and cloud radiative properties [37]. Although volcanic aerosol sources are weak compared to other aerosol sources, the sulphur compounds emitted during eruptions may have a large effect on the planetary radiation budget as the sulphur compounds from anthropogenic emissions [38]. This is because volcanic eruptions can eject particles very high into the atmosphere where they may remain for a long time [38, 39].

Anthropogenic Aerosols

Anthropogenic aerosols consist of both primary particles (e.g., diesel exhaust and dust, see Fig. 1.4) and secondary particles formed from gaseous anthropogenic emissions. Anthropogenic aerosols contribute substantially to the radiative forcing of the Earth's climate both directly through absorption and scattering of solar radiation and through modification of cloud optical properties [4]. They contribute about 10% of the total aerosol loading but these emissions did not exist in the pre-human era [7]. The influence of this small but ever growing contribution on the climate system is not well documented and must be assessed in atmospheric studies.

1.1.2 Effects of Aerosols on Climate

Atmospheric aerosols interact both directly and indirectly with Earth's radiation budget and thus influence the climate. The direct way is by scattering and absorption of solar radiation in the Earth's atmosphere. Aerosols counteract part of the warming effect of greenhouse gases by increasing the amount of sunlight backscattered into space. However, absorption of sunlight by aerosols warms the aerosol layer and this modifies the relative humidity conditions and thus affecting the process of cloud formation (the semi-direct effect) [41]. Absorption by particles heats up the atmosphere

Figure 1.4: A hazy atmosphere due to gaseous particles released during combustion of fossil fuels from cars. Reprinted from Nature [40].

while backscattering of sunlight into space cools the atmosphere. This makes absorption and backscattering of sunlight the most important optical properties of atmospheric aerosols in relation to climate change. Aerosols exist in two distinct atmospheric layers, the troposphere, i.e., from the surface of the Earth up to about 10 to 20 km, and the stratosphere, i.e., between about 10 – 20 and 50 km. The troposphere is thermally coupled to the Earth's surface whereas the stratosphere is not. Because of their thermal isolation, stratospheric particles tend to cool the Earth's surface both by backscattering and absorption of solar radiation [3].

The thermal infrared effects of particles are also important, especially in the 8 – 12 μm window region, where the major atmospheric gases are highly transparent. This is the wavelength region where the Planck function peaks for normal terrestrial temperatures [3]. The upwelling infrared radiation from the Earth's surface is therefore partly hindered from escaping into space because some particles are strongly absorbing in this spectral region [3]. Thus aerosols contribute to the greenhouse effect. Infrared radiation emitted towards the Earth's surface by stratospheric particles may cause some warming in the lower atmosphere, thereby countering to some extent the cooling caused by backscattering and absorption of solar radiation.

Indirectly, aerosols in the lower atmosphere modify the cloud micro-physics and this affects the radiative properties, amount, and lifetime of clouds. Each cloud droplet requires an aerosol particle to act as a cloud nuclei to condense upon. Therefore the concentration, size, and composition of aerosols that can act as CCN determine the cloud properties, evolution, and development of precipitation [42]. But the availability of moisture, up drafts and cloud formation are influenced by large scale dynamic processes. Natural aerosols are important for cloud formation but anthropogenic aerosols (urban haze) and smoke aerosols may seem to have a negative effect towards cloud formation and thereby affecting precipitation and cloud radiative properties [37, 43]. Studies have shown that anthropogenic aerosols and smoke lead to reduced cloud droplet size and delay the onset of precipitation [43–45].

Without aerosol particles, cloud formation would not occur in the atmosphere at the temperatures and relative humidities at which clouds are observed to exist. Pure water droplets can form from the vapor phase only at very high super saturations, i.e., at par-

tial pressures well above the equilibrium vapor pressure for water at a given temperature [46]. The presence of aerosols in the atmosphere provides nuclei onto which liquid water or ice can condense at much lower partial pressures, initiating droplet formation and eventually allowing the nuclei to grow to sizes recognized as cloud particles. In the same process, the incorporation of aerosols into cloud water and precipitation is the main mechanism of removing aerosols from the atmosphere [47].

The way in which aerosols affect climate through their interaction with clouds and hence precipitation are complex, and current climate models have not helped to solve the controversy. And as a result, the radiative forcing caused by anthropogenic aerosols on climate systems is highly uncertain, making it difficult to discern and predict the extent of global warming [48]. For example, it has been revealed that changes in the cloud-aerosol concentration can alter the precipitation efficiency of clouds, thereby changing cloud amount and hence, the radiative forcing of the climate [49]. Other situations may be hypersensitive to aerosols because aerosols have become extremely depleted by precipitation [50]. In these ultra-clean regimes, addition of aerosols can dramatically increase cloud cover, causing a large cooling [51].

Finer aerosol particles with sizes close to the wavelengths of visible light are expected to have a stronger climatic impact than larger aerosol particles [2]. The reflection of sunlight by aerosols cools the climate system. But depending on their composition, aerosols can also absorb solar radiation in the atmosphere, which will cool the surface but warms the atmosphere in the process. These effects of aerosols on the temperature, and also the role of aerosols as CCN, impact the hydrological cycle, through changes in cloud cover, cloud properties and precipitation [37]. Because aerosols have different shapes and forms, ranging from dust to urban pollution, and also the strong variability of aerosol concentrations over time and space, it is difficult to understand how aerosols influence climate.

Accurate knowledge of aerosol distribution and composition requires continuous observations from satellites, networks of ground based instruments and dedicated field experiments. It is also important to note that increase in aerosol concentration and changes in aerosol composition, due to industrialization and expanding population, may have adverse affects on the Earth's climate and water supply [37].

1.1.3 Characterization of Atmospheric Aerosols

Spectral aerosol optical thickness AOT(λ) and precipitable water vapor column (PWVC) are two very important physical parameters for characterizing aerosols. Routine observation of the AOT(λ) and the PWVC globally is a fundamental way of determining aerosol optical characteristics and aerosols influence on the global radiation budget and climate change [52]. Accurate knowledge of the spatial and temporal extent of AOT(λ) and aerosol properties is important for assessing their influence on satellite measurements [53].

The impact of aerosols on climate is not well known and it is considered as one of the largest uncertainties in climate modelling. One of the main reasons for this uncertainty is the lack of measurements on global scale. Ground-based measurements with significant temporal coverage are only available at a few locations [54]. To fully understand aerosols influence on climate radiative forcing one requires constant validation and augmentation by ancillary ground-based observations as can be provided

by sun photometers [55]. Appropriate and accurate instrument calibration of ground-based sun photometers is required in order that absolute atmospheric parameters can be retrieved from their measurements with an acceptable uncertainty [56].

1.2 Solar Radiation

The elliptic nature of the Earth's orbit around the Sun causes a seasonal variation of the Earth-Sun distance of about 3.4% from its minimum value in January to its maximum value in July. Since the irradiance is inversely proportional to the square of the distance, the variation of about 3.4% in the Earth-Sun distance causes a variation of about 6.9% between the minimum and maximum values of irradiance at the top of the atmosphere (TOA).

The extraterrestrial solar radiation exhibits some temporal variations such as the 11 year solar cycle of sunspots and occasional flares. Such variations affect mostly the shorter wavelengths of the spectrum, and are completely absorbed by atmospheric ozone and therefore do not reach the Earth's surface. The amount of solar radiation reaching the Earth's surface depends on the solar zenith angle, and the optical properties of the atmosphere.

1.2.1 Ultraviolet Solar Radiation

The atmospheric transmission of ultraviolet (UV) radiation is determined by the total ozone column (TOC) and the amount of suspended particles (clouds and aerosols). The UV radiation has significant effects on living organisms due to its high photon energy [57, 58]. Small and controlled amounts of UV radiation are essential in the production of vitamin D in humans and can be used to treat some diseases such as rickets and psoriasis. But prolonged exposure to high UV radiation doses may result in acute and chronic health effects on the skin, eye, and immune system [59].

The UV radiation spectrum is divided into three parts: UV-C radiation (200 – 280 nm), UV-B radiation (280 – 315 nm), and UV-A radiation (315 – 400 nm). The UV-C radiation is totally absorbed by oxygen and atmospheric ozone because of its high energy, which causes production (see Eq. (1.3)) and destruction (see Eq. (1.4)) of ozone in the stratosphere and troposphere [58–60].

Figure 1.5 shows that the UV-C energy decreases dramatically as ozone increases because of the strong absorption in the 200 – 280 nm wavelength band. The UV-B is also strongly absorbed, but a small fraction reaches the Earth's surface. The UV-A is only weakly absorbed by ozone, with some scattering of radiation near the Earth's surface.

About 90% of the UV-B radiation is absorbed by atmospheric ozone so that only about 10% reaches the Earth's surface, and it is responsible for the skin erythema [58–60]. The UV-B radiation causes damage at the molecular level to the fundamental building block of life, deoxyribonucleic acid (DNA). The DNA readily absorbs UV-B radiation, which commonly changes the shape of the molecule in one of several ways as illustrated in Fig. 1.6 [61]. And such changes in the DNA molecule often mean that the protein-building enzymes can not "read" the DNA code at that point on the molecule [61].

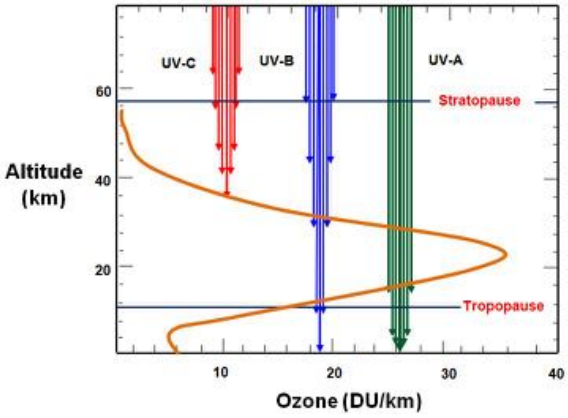

Figure 1.5: The vertical ozone profile for mid-latitude. UV radiation as a function of altitude for UV-C (red), UV-B (blue), and UV-A (green) are also shown on the graph. The width of the bar indicates the amount of energy as a function of altitude.

The UV-A radiation is nearly insensitive to ozone and represents most of the UV radiation energy received at the Earth's surface [58–60]. Therefore, it is expected that variability of atmospheric ozone, clouds, and aerosols will lead to variability of UV-A and UV-B radiation at the Earth's surface, whereas the UV-C radiation will be totally absorbed by oxygen and atmospheric ozone.

Rayleigh scattering by air molecules also affects the amount of UV-B and UV-A reaching the Earth's surface. Rayleigh scattering is inversely proportional to the fourth power of the wavelength of incident light. This type of scattering is valid only if the wavelength of the incident light is much smaller than the size of the scattering particle. Because of the strong wavelength dependence of Rayleigh scattering, the ratio of diffuse to global radiation for clear-sky conditions is larger for UV-B than for UV-A.

Cloud cover can significantly affect UV radiation at the Earth's surface due to strong scattering. This type of scattering is called Mie scattering and is strong in the forward direction. It has a weak wavelength dependence and similarly scatters both UV-B and UV-A.

1.2.2 Erythemal UV Radiation

Erythemal UV radiation is the irradiance (Wm^{-2}) measured over the 280 through 400 nm range and weighted with the McKinlay and Diffey [63] action spectrum. Although the absorption in the UV-B region (280 – 315 nm) is weak, any increment in the UV-B radiation may lead to substantial biological effects due to exposure to UV radiation [57, 58].

The biological effects can be estimated by multiplying the UV irradiance with a spectral sensitivity function (action spectrum), and the product is integrated over the UV spectral range [64, 65]. If $F(\lambda)$ is the irradiance at wavelength λ and $A(\lambda)$ is the

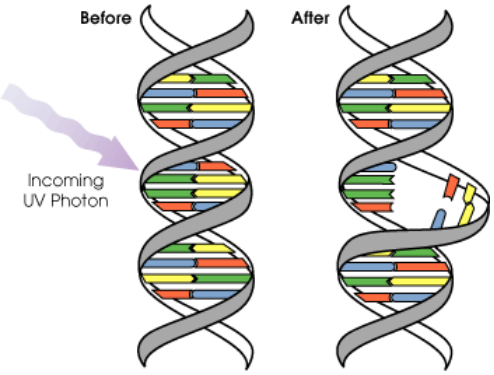

Figure 1.6: UV photons harm the DNA molecules of living organisms in different ways. In one common damage event, adjacent bases bond with each other, instead of across the "ladder." This makes a bulge, and the distorted DNA molecule does not function properly. Reprinted from [62].

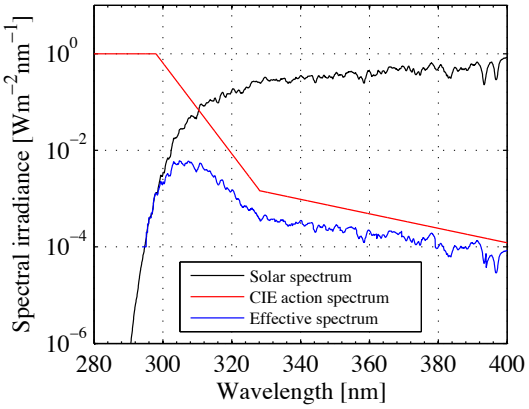

Figure 1.7: Sunburn effect or the UV index (area under the blue curve) is the product of the sunlight power spectrum (black curve) and the erythemal action spectrum or skin susceptibility to erythema (red curve) across the range of UV wavelengths [63]. The solar spectrum was calculated at a solar zenith angle of 0° using AccuRT code.

biological action spectrum, then the erythemal UV irradiance UV_E is defined as

$$UV_E = \int_{250\text{ nm}}^{400\text{ nm}} A(\lambda)F(\lambda)d\lambda. \tag{1.1}$$

For erythema, the biological action spectrum $A(\lambda)$ is the widely used CIE action spectrum defined below [63], and shown with the green curve in Fig 1.7. The CIE action spectrum is a model for the susceptibility of the skin to sunburn (erythema). It is proposed by McKinlay and Diffey [63] and adopted as a standard by the Commission

Internationale de l'Éclairage (CIE).

$$A(\lambda) = \begin{cases} 1 & 250 < \lambda \leq 298 \text{ nm} \\ 10^{0.094(298-\lambda)} & 298 < \lambda \leq 328 \text{ nm} \\ 10^{0.015(139-\lambda)} & 328 < \lambda \leq 400 \text{ nm} \\ 0 & 400 \text{ nm} < \lambda. \end{cases}$$

The erythemal UV irradiances can be used to calculate a unit less value called erythemal UV index. The erythemal UV index or simply the UV index is an estimation of the UV levels that are important for the effects on the human skin. It is an artificial quantity derived from the erythemal UV irradiances. The UV index is defined by the World Meteorological Organization as,

$$UVI = 40 \times UV_E, \tag{1.2}$$

where UVI is the UV index and UV_E is the CIE weighted UV erythemal irradiance (in Wm^{-2}) [59]. The UV index values are largest in the tropics (close to the Equator) and are smallest at the poles (see Fig. 1.8).

1.2.3 Stratospheric Ozone Layer

Ozone is a gas made up of three oxygen atoms (O_3). It occurs naturally in small (trace) amounts in the upper atmosphere (the stratosphere) at an altitude of about between 10 and 50 km. Anthropogenic aerosols such as vehicle exhaust and gasoline vapors are responsible for the creation of ozone in the troposphere close to the Earth's surface, and yet high concentrations of ozone are toxic to humans, animals, and plants [67].

Ozone is naturally formed and destroyed in the stratosphere through a photochemical process involving oxygen and solar UV radiation [68]. When molecular oxygen (O_2) absorbs UV radiation of wavelength below 242 nm, the chemical bond is broken to produce atomic oxygen (O) which bonds with molecular oxygen (O_2) to form ozone (O_3) [68].

$$\begin{aligned} \text{O}_2(\text{g}) + h\nu &\longrightarrow 2\text{O}(\text{g}), \\ \text{O}(\text{g}) + \text{O}_2(\text{g}) &\longrightarrow \text{O}_3(\text{g}). \end{aligned} \tag{1.3}$$

Ozone is destroyed by absorption of UV radiation of wavelength below 310 nm. An ozone molecule combines with an oxygen atom to form two oxygen molecules, or through certain chemical reactions involving molecules containing hydrogen, nitrogen, chlorine, or bromine atoms.

$$\text{O}_3(\text{g}) + h\nu \longrightarrow \text{O}_2(\text{g}) + \text{O}(\text{g}) \tag{1.4}$$

$$\text{O}_3(\text{g}) + \text{O} \longrightarrow \text{O}_2(\text{g}) + \text{O}_2(\text{g}). \tag{1.5}$$

The atmosphere maintains a natural balance between solar UV radiation that creates ozone and chemical reactions that destroy ozone. However, the production of chlorofluorocarbons (CFCs) which are used as refrigerants, solvents, and propellants, have altered the natural balance of chemicals in the stratosphere [67]. The CFCs are non-reactive chemicals and because of this, they tend to build up high in the stratosphere where they are eventually destroyed by the UV radiation. Their destruction

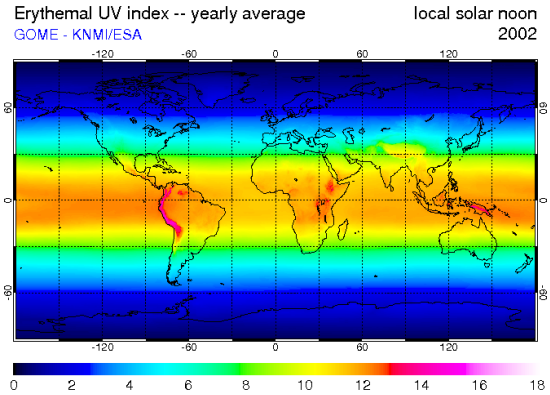

(a)

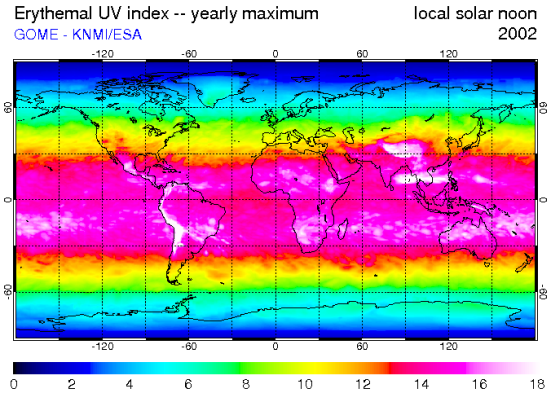

(b)

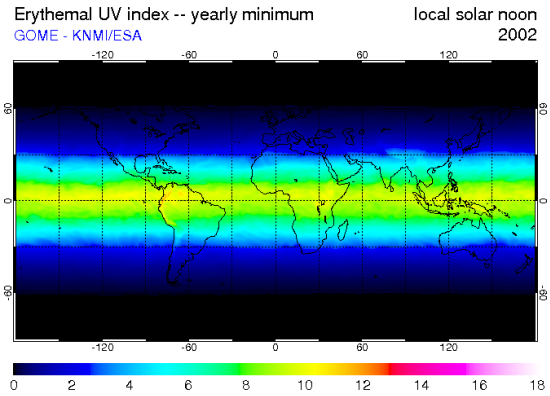

(c)

Figure 1.8: Solar noon erythemal UV index values derived from GOME satellite data for the year 2002; (a) yearly average, (b) yearly maximum, and (c) yearly minimum. Reprinted from the Royal Netherlands Meteorological Institute (KNMI) and the European Space Agency (ESA) [66].

however, results in free-floating chlorine atoms, which play an active role in the destruction of ozone molecules. In a similar way, anthropogenic gases such as nitrous oxide and bromine compounds, are broken down in the stratosphere and play active roles in ozone destruction [69]. For that reason therefore, CFCs were banned by the United Nations (UN) under the Montreal Protocol, and were replaced with other products such as hydro fluorocarbons (HFCs) which do not damage the ozone layer, but could lead to global warming [70].

In the troposphere, the CFCs are so stable and they can persist for a long time, e.g., for years or even decades. Because of this long term persistence, some of the CFCs can eventually escape into the stratosphere, where the UV radiation can break the bond holding chlorine atoms to the CFC molecule. The freed chlorine atom can then participate in a series of chemical reactions that destroy ozone and return the free chlorine atom to the atmosphere unchanged, where it can destroy more ozone molecules [67].

The destruction of ozone by free chlorine atoms is a process and it does not happen immediately. The free chlorine atoms that are separated from the CFCs react with other chemical compounds to form either hydrochloric acid or chlorine nitrate. Under normal atmospheric conditions, hydrochloric acid and chlorine nitrate are so stable and are considered as long-term reservoirs for chlorine. During the polar winter over the Antarctica, the atmospheric conditions are unusual, and an endlessly circling whirlpool of stratospheric winds (the polar vortex) isolates the air in the center. And because of the total darkness, the air in the vortex gets so cold that clouds form, even though the Antarctic air is too thin and dry. Under these atmospheric conditions, some chemical reactions take place that could not have happened anywhere else in the atmosphere. The unusual reactions occur only on the surface of polar stratospheric cloud particles, which may be water, ice, or nitric acid, depending on the temperature. Figure 1.9 shows one of such cases during which frozen crystals of the polar stratospheric clouds provide a surface for the reactions that free chlorine atoms in the atmosphere over the Antarctica [71].

Figure 1.9: Thin nacreous clouds made of mixtures of ice, nitric acid, and sulphuric acid form in the polar stratosphere when temperatures drop below -88 °C. In such polar stratospheric clouds, active form of chlorine are released from their reservoirs. Its beautiful colors result from the diffraction of light by ice crystals. Ozone depletion occurs in such polar stratospheric clouds. Reprinted from NASA Goddard Space Flight Center [67].

The unusual reactions convert the inactive chlorine reservoir chemicals (hydrochlo-

ric acid and chlorine nitrate) into more active forms (e.g., chlorine gas). When sunlight returns to the Antarctica in October, UV radiation rapidly breaks the bond between the chlorine atoms, releasing free chlorine into the stratosphere. The free chlorine then participates in reactions that destroy ozone molecules while regenerating the chlorine, in a reaction process known as a catalytic reaction (see Fig. 1.10). The catalytic reaction allows a single chlorine atom to destroy thousands of ozone molecules. The ozone hole grows throughout the early spring until temperatures increase and the polar vortex weakens, ending the isolation of the air in the polar vortex. As warm air from the surrounding latitudes mixes into the polar region, the atmospheric conditions that favour chemical reactions that lead to ozone destruction, are dispersed. The ozone layer stabilizes until the following spring [71].

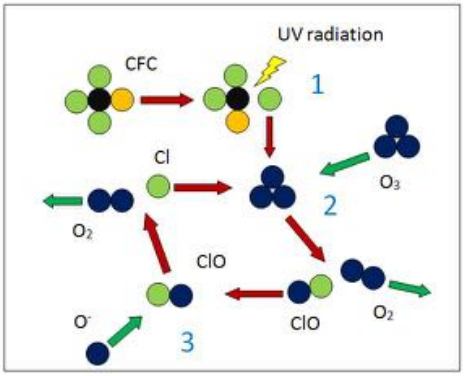

Figure 1.10: Catalytic destruction of ozone by chlorine in the stratosphere. UV radiation breaks off a chlorine atom (green) from a CFC molecule. The free chlorine atom attacks and destroys an ozone molecule to form an oxygen molecule and a chlorine monoxide molecule. The chlorine monoxide molecule is attacked by a free oxygen atom to release the chlorine atom and form an oxygen molecule. The chlorine atom is then free to attack another ozone molecule and repeat the destructive process.

1.3 Atmospheric Data Sampling Techniques

The method or technique used to sample the atmosphere is of great importance in atmospheric monitoring. The sampling techniques are divided into two main categories and they include, point sampling methods also known as *in situ* sampling and remote sampling. *In situ* sampling methods measure the atmosphere at a single localized point. Such methods require the instrumentation to be located at the same point and in contact with the atmospheric compound to be measured [73, 74]. They are often fixed, though may be mounted on a mobile platform such as a balloon or an aircraft.

Remote sensors on the other hand measure the concentration of atmospheric compounds at a location or distance away from the subject of interest. Remote samplers are either passive or active systems. Passive instruments receive information naturally emitted from a region in the atmosphere whereas active instruments emit either an acoustic or electromagnetic signal and record the characteristics of this signal after it

interacts with an object or surface and returns back to the sensor [73]. Remote sensing techniques used in atmospheric monitoring generally employ optical or microwave radiation, and acoustic sounders to probe the atmosphere. Also systems that measure the path integral concentration of a gas along a sensing beam, known as long path or open path sensors, are included in this category [74].

1.3.1 Ground-based Measurements

Ground-based and satellite remote sensing measurements have been used in this thesis. The ground-based measurements were taken with well calibrated multichannel filter instruments. Such measurements require detailed instrument characterization and accurate calibration in order to provide high quality data necessary for validation of satellite data. Different types of instruments are used for such purposes and they include, spectroradiometers, multichannel radiometers, and broadband radiometers. Though spectroradiometers present the highest resolution, they are often very expensive and as a consequence most ground-based stations use multichannel and broadband radiometers. The multichannel and broadband radiometers can reproduce the wavelength integrated quantities as accurately as the spectroradiometers if they are well calibrated [75].

1.3.2 Satellite Remote Sensing

Several satellite instruments have been launched into space by different space agencies, such as NASA, ESA, the Japanese Aerospace Exploration Agency, KNMI, and many others. The high spatial and temporal resolution of such instruments makes satellite remote sensing data more valuable in oceanography and atmospheric studies. Satellite instruments are equipped with sensors capable of detecting emitted, back-scattered or reflected solar radiation both in the visible and infrared regions of the spectrum. Satellite remote sensing has helped to explain major pollution, dust, smoke, and volcanic events in stunning detail since atmospheric aerosols are well suited for satellite remote sensing [76]. With the sun as a stable light source, the light scattered by aerosols can easily be detected by high resolution spectral radiation sensors on board the satellites.

The current satellites orbiting the Earth are either in geostationary or polar orbits (see, Fig. 1.11). Geostationary satellites are orbiting the Earth in the equatorial plane at a distance of about 36,000 km above the surface. The satellite's rotational velocity is identical to that of the Earth, and this enables the monitoring of dynamic meteorological phenomena such as major dust clouds, volcanic eruptions, smoke plumes or regional pollution events as they evolve throughout the day [76].

Polar satellites are orbiting the Earth in a plane that passes through the two poles. The orbit is adjusted to about 100 km above the Earth's surface and this corresponds to a full rotation every after 90 minutes. Due to the low orbit, each consecutive rotation samples only a swath of the Earth's surface that is at most 3000 km wide. Each swath is incremented such that the polar orbit is sun-synchronous, i.e. the sensor will always observe the sunny side of the Earth at the same local time of the day. But this limits the polar orbiting satellite to only one measurement or observation per day of any given location on the Earth's surface. The low orbit permits sensors to have higher spatial resolution and geo-location accuracy. Most quantitative aerosol data sets and clima-

tologies are derived from polar orbiting satellites carrying a variety of sensors [76].

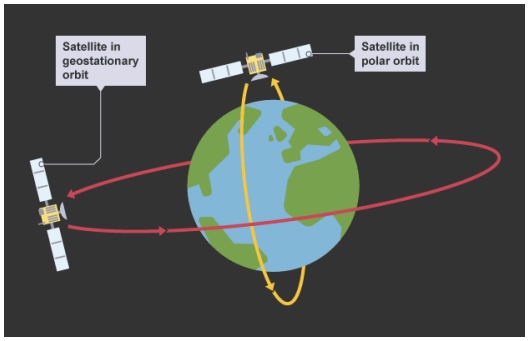

Figure 1.11: Two types of satellite orbits, geosynchronous (red) and polar orbits (yellow). Picture is reprinted from the BBC [77].

There are two basic observation modes for satellite instruments depending on the observation geometry, i.e., vertical and horizontal observation modes (see Fig. 1.12). In vertical (or nadir viewing) observation mode, the satellite instrument faces to nadir or near-nadir to detect and measure the radiation coming from the Earth. A number of satellite instruments use the vertical observation concept to provide column integrated products. Observations in horizontal direction including Limb-viewing and occultation sounding, probes the Earth's limb at various depths in the atmosphere. Horizontal observations are characterized by altitude and geo-location of the tangent point. Sun occultation instruments can retrieve aerosol extinction profile from measurements of solar extinction through the atmospheric limb during sunrise and sunset [78].

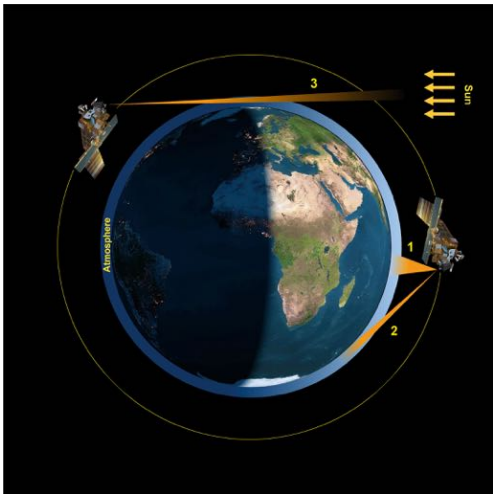

Figure 1.12: Different satellite observation modes. (1) nadir (vertical), (2) limb, and (3) occultation (horizontal). Reprinted from ESA [79].

1.4 Objectives of this Study

The main aims of this thesis were to investigate aerosols and aerosol optical properties, and to study UV radiation using both ground-based measurements and satellite remote sensing. We were interested to know how aerosols affect UV radiation especially in areas with high UV radiation. Our specific objectives were;

- To investigate aerosols and their properties in the atmosphere of Bergen, Norway.
- To study aerosols and UV radiation in the African belt using satellite remote sensing.
- To analyse and study aerosol optical properties using AERONET measurements in Norway.
- To validate satellite remote sensing measurements using ground-based measurements in Kampala, Uganda.

By the time we finished writing this thesis we had achieved a great deal of our objectives. Although some more questions were raised during this study, we hope to answer them in the future studies.

Chapter 2

Instrumentation

We used data from two ground-based instruments, i.e., the NILU-UV instrument which was used to measure UV irradiances at a ground-based UV station in Kampala, and the CIMEL sun/sky photometers which were used for aerosol measurements in Norway. Solar UV irradiances were also measured from space by two satellite instruments, i.e., the total ozone mapping spectrometer (TOMS) and the ozone monitoring instrument (OMI).

2.1 The NILU-UV Irradiance Meter

Figure 2.1: The NILU-UV instruments during a field trip at Røst, northern Norway in July, 2012. The instrument is robust and can be seen being used in both wet and dry weather conditions.

The Norwegian Institute for Air Research UV (NILU-UV) irradiance meter is a multi-channel, moderate bandwidth filter instrument, manufactured by Innovation NILU AS, Kjeller, Norway. The NILU-UV is an accurate, reliable, and robust instrument for measuring irradiances at UV and visible wavelengths. It consists of a teflon diffuser, silicon detectors, and high quality bandpass filters.

The teflon diffuser reduces the angular sensitivity of the incoming solar radiation. After passing through the teflon diffuser, the incoming radiation is passed through high quality bandpass filters with very low out-of-band transmittance. The filtered light is then converted into electric currents by the photo-detectors, one for each channel. The electric currents are subsequently amplified, digitized within the instrument, and converted to absolute irradiances for each channel.

As described by Høiskar et al. [80], the instrument has six spectral channels, five of which are in the UV spectral region with center wavelengths at 302, 312, 320, 340, and 380 nm and bandwidths of approximately 10 nm at full width half maximum (FWHM). The sixth spectral channel covers the visible range of the spectrum (400 – 700 nm) and measures the photosynthetically active radiation (PAR) [80].

The NILU-UV instrument records and stores data in a built-in data logger with one minute time resolution. The data logger has the capacity to store 3 weeks of one-minute averages of the measured irradiances. The stored data can be transferred to a computer using a built-in RS-232 port. The measurements obtained with a NILU-UV instrument can be used to provide CIE weighted UV-dose rates, integrated UV-A and UV-B irradiances, cloud cover assessment, TOC values, and integrated PAR irradiances.

2.2 The CIMEL Sun/Sky Photometers

Aerosol data was measured with multi-band CIMEL sun/sky photometers, manufactured by CIMEL Electronique, 172 Rue de Charonne, 75011 Paris, France. Two types of CIMEL instruments were used to measure aerosol data used in this study, i.e., CIMEL CE317 and CIMEL CE318. These are generally the same instruments only that the CIMEL CE317 is a hand-held instrument which is pointed towards the Sun and directed by hand to take measurements. The CIMEL CE318 is one of the instruments used by the Aerosol Robotic Network (AERONET). It is an automatic instrument with a robotic arm which helps it to take measurements without any human help.

2.2.1 The CIMEL CE317 Instrument

The instrument is equipped with up to six interference filters selected between 400 to 1040 nm. It consists of a metal casing to protect it from bad weather and water, and has a built in battery that can power it for many days without recharging depending on the number of measurements made per day. It has a sensor head equipped with 1 collimator aiming angle of 1° field of view for the measurement of the direct sun radiance or 5° field of view for sky radiance. It consists of a thermistor for measuring the temperature of the detector allowing compensation for any temperature dependence of the silicon detector [81].

The CIMEL instrument may be mounted on a tripod and directed by hand towards the sun or sky. The instrument measures direct solar irradiance from which the spectral total optical thickness (TOT) $\tau(\lambda)$ can be retrieved. The data is stored in a memory and can easily be transferred in an ASCII file to a computer. The memory is big enough to store data from several measurements made for several days before being transferred to a computer [81]. The spectral band filters limit the amount of sunlight reaching the

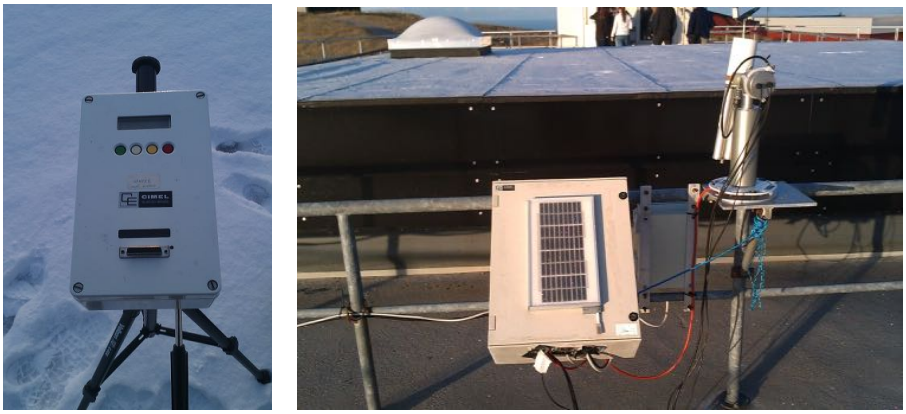

(a) (b)

Figure 2.2: The CIMEL sun/sky photometers (a) CIMEL CE317 portable instrument and (b) CIMEL CE318 instrument at an AERONET site at Andøya, Andenes, northern Norway. The instrument is observed in park position with the sensor head pointing nadir to avoid damage and contamination of the sensor by water, dust or snow while not in use.

photo-sensitive detector to strictly 440, 670, 870, 936, 940, and 1020 nm wavelengths each with a bandwidth of about 10 nm. These spectral interference filters are arranged on a rotating wheel which rotates inside the instrument to click into position a given filter in order to take a measurement for that particular filter. The measured data can be used to retrieve the PWVC and spectral AOT, aerosols properties study, sky radiance, and atmospheric corrections of satellite data (e.g., AVHRR, METEOSAT) [81].

When placed somewhere on the Earth's surface or in the atmosphere, the sun photometer's measured irradiance is not equal to the irradiance emitted by the sun (the extraterrestrial solar irradiance). The solar flux is reduced by atmospheric absorption and scattering (see Fig. 2.3). The measured flux is a combination of what is emitted by the sun and the effect of the atmosphere. These quantities (extraterrestrial, atmosphere and the measured) are related through the Beer-Lambert-Bouguer's law. The atmospheric effect is removed by the Langley extrapolation method which makes it easy to determine the extraterrestrial solar irradiance with the ground-based measurements. When the extraterrestrial solar irradiance is known, we can use the sun photometer to study the atmosphere. The atmospheric TOT ($\tau(\lambda)$), AOT (τ_A), PWVC and other optical properties of the atmosphere can be determined. We subtract off, the Rayleigh scattering component (τ_R) and the component due to ozone (O_3) absorption (τ_{Oz}) from the atmospheric TOT (τ) to get the AOT (τ_A) (see Eq. (2.1)). The contribution to the TOT by other trace gases such as nitric oxides are considered negligible.

$$\tau_A(\lambda) = \tau(\lambda) - \tau_R(\lambda) - \tau_{Oz}(\lambda) \tag{2.1}$$

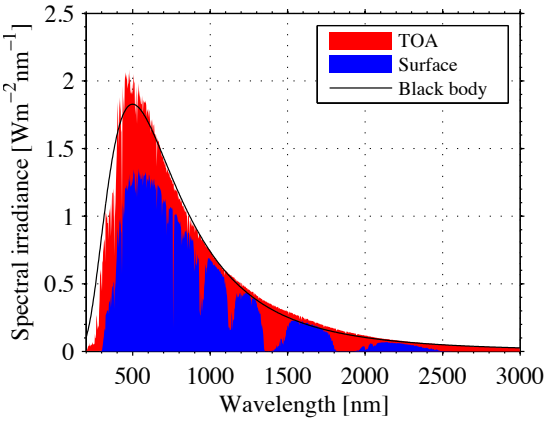

Figure 2.3: The solar radiation spectrum at the top of the atmosphere (red) and at the Earth's surface (blue) calculated at a solar zenith angle of 0° using AccuRT code. The black curve represents the spectrum if the sun were to radiate as a black body at a temperature of about 5800 K (note that the values are multiplied by 6.8×10^{-5} sr, the solid angle of the solar disk). The spectrum at the surface of the Earth or at sea level, has several broken parts due to absorption by and molecules in the atmosphere.

2.2.2 The Aerosol Robotic Network

The AERONET, is a ground-based global network of sun and sky radiometers that operates at more than 800 sites worldwide [55]. The network offers a standardization for ground-based regional to global scale aerosol monitoring and characterization. Routine observations are performed by programmable and automatic sun and sky radiometers. The AERONET's aerosol measurements are quality assured and are screened to be cloud-free [55, 82].

The main instrument used at AERONET sites is a CIMEL sun and sky spectral radiometer (CE318), seen in Fig. 2.2(b). It is an automatic instrument with a robotic arm that enables it to make measurements without human help. The instrument is weather handy and solar powered making it a good field instrument. It has two collimators each 33 cm long and having approximately 1.3° full-angle field of view, one for direct sun radiance and the other for sky radiance measurements. The spectral interference filters are arranged on a motor driven wheel with center wavelengths at 340, 380, 440, 500, 675, 870, 937, 1020, and 1640 nm. It consists of a thermister that measures the temperature of the detector allowing compensation for any temperature dependence in the silicon detector.

To make measurements, the sensor head is pointed by stepping azimuth and zenith motors with a precision of 0.05°. The microprocessors then compute the position of the sun based on time, latitude, and longitude, which directs the sensor head to within approximately 1° of the sun. After that a four quadrant detector precisely tracks the sun before a programmed measurement sequence begins. The "almucantar" technique is used to measure sky radiances. After the routine measurement is completed, the instrument returns to the "park" position awaiting the next measurement sequence [55,

81].

On a clear-sky day, a sequence of 6 measurements of both direct sun and sky radiances are automatically performed. The measurements are canceled if the "wet sensor" of the spectral radiometer is exposed to precipitation. The measured data from the memory is then transferred to a computer or via the Data Collection System of AERONET to one of the three geostationary satellites; GOES, METEOSAT or GMS, and then transmitted from the satellite to the ground receiving station [55, 81]. The spectral radiometer's measurements are used to retrieve the AOT, the single scattering albedo, size distributions, bimodal fractions, scattering phase function, and asymmetry factor.

2.3 Satellite Instruments

Satellite remote sensing observations are commonly used to monitor and study the temporal and spatial variations of UV radiation, aerosols, and TOC, on both local and global scales. Such observations provide a global view of the Earth's atmosphere over extended periods of time with sufficient spatial resolution allowing the detection of local, regional, and global trends of aerosols, UV radiation, and TOC. A series of space missions with instruments capable of making observations of backscattered solar radiation emerging at the TOA, have been launched since the late 1970s.

2.3.1 The Total Ozone Mapping Spectrometer

The TOMS instrument was one of the many (about eight) instruments designed to provide continuous and long-term monitoring of atmospheric, oceanic and surface parameters on a global basis aboard the Nimbus-7 spacecraft during the 1980s. The Nimbus-7 spacecraft's TOMS instrument operated between November 1978 and May 1993 [83]. Several experiments related to pollution, oceanography, and meteorology were conducted on the Nimbus-7 platform. The Nimbus-7 Observatory's equatorial crossings were local noon for ascending node and local midnight for descending node. The ascending node is where the satellite crosses the equator going from south to north, and the descending node is where it crosses the equator going from north to south.

For the purpose of obtaining daily high resolution global coverage of the Earth's TOC, the TOMS instrument measures the UV albedo, i.e., the ratio of backscattered to incoming solar irradiance, in six selected wavelength bands [83, 84]. The experiment (TOMS) uses a single monochromator and scanning mirror to sample the backscattered solar UV radiation at 35 sample points at 3° intervals to 51° on each side of the subsatellite point, in a direction perpendicular to the orbital plane. Consecutive cross-scans overlap, creating a contiguous mapping of ozone. The measurements made during the satellite's ascending node are used for the TOC retrievals [83]. The mission was successful in mapping to the detail of the global TOC distribution as well as the Antarctic ozone hole, which forms between September and November every year.

2.3.2 The Earth Probe TOMS

The Earth Probe's TOMS (EP-TOMS) was the only instrument aboard an Earth Probe Spacecraft that was launched on July 2, 1996. It continued NASA's long-term daily mapping of the global distribution of the atmospheric TOC, that began with Nimbus 7 Satellite in 1978 and continued with the TOMS instrument aboard a Russian Meteor-3 Satellite which stopped working in December 1994 [84].

The data is used to monitor the long-term trends in the TOC and seasonal chemical depletions of ozone which occur during polar spring at both the southern and northern hemispheres. The EP-TOMS monitoring capabilities also include the detection of smoke from biomass burning, identification of desert dust and other aerosols as well sulfur dioxide and ash emitted by large volcanic eruptions [84].

The EP-TOMS algorithm is identical to the one used by the Nimbus 7 and Meteor 3 TOMS instruments. A radiative transfer model is used to calculate backscattered radiances as a function of TOC, latitude, viewing geometry, and surface albedo. The TOC values are then derived by comparing measured radiances with theoretical radiances calculated for the conditions of the measurement and finding the value of TOC that gives a computed radiance equal to the measured radiance [84].

2.3.3 The Ozone Monitoring Instrument

The OMI is a high spectral resolution UV and visible (270–500 nm) spectrometer. It is one of the four instruments aboard the NASA's Aura spacecraft, shown in Fig. 2.4. The four instruments onboard the Aura spacecraft are: the OMI, High Resolution Dynamics Limb Sounder (HIRDLS), Microwave Limb Sounder (MLS), and Tropospheric Emission Spectrometer (TES). The Aura mission is part of NASA's Earth Observing System that was launched in July 2004 [85–87]. The Aura spacecraft describes a sun-synchronous polar orbit with ascending node equator crossing time at 13:45 local time [85, 87]. The OMI has a 2600 km wide swath and it provides daily global coverage at a spatial resolution varying from 13 km $\times$ 24 km at nadir to 28 km $\times$ 150 km at the extremes of the swath [86], as shown in Fig. 2.5.

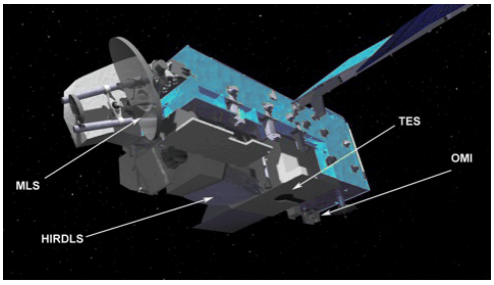

Figure 2.4: A model of Aura spacecraft showing the locations of the four onboard instruments, HIRDLS, MLS, OMI, and TES. Reprinted from [87].

The surface UV algorithm applied to OMI data is regarded as a continuation of the TOMS UV algorithm developed by NASA's Goddard Space Flight Center [87, 88]. The

OMI combines the advantages of its predecessors, the Global Ozone Monitoring Experiment, Scanning Imaging Absorption Spectrometer for Atmospheric Chartography, and TOMS and measures the complete solar spectrum in the UV and visible spectral ranges with high spatial resolution (13×24 km^2) and daily global coverage [85, 87]. It continues the TOMS record of high-quality TOC measurements and monitors the stratospheric ozone recovery that was predicted by chemical models [89]. The OMI measurements are inputs to inversion algorithms used to retrieve TOC values, cloud and AOT, and total column amounts of trace gases, such as NO_2, SO_2, HCHO, BrO, and OClO [85, 86]. The OMI surface UV irradiance algorithm is used to estimate erythemally or CIE weighted daily doses and erythemal dose rates at local solar noon [86].

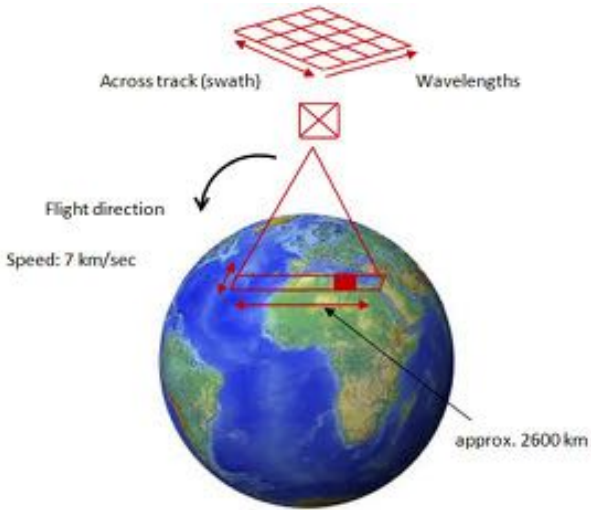

Figure 2.5: OMI measurement principle.

Clear-sky surface UV irradiances are estimated using TOC values inferred from OMI measurements and climatological surface albedo values [90]. The estimated surface UV irradiances are reprocessed using a transmittance factor that accounts for attenuation of UV radiation by non-absorbing clouds and aerosols [91]. The ratio of backscattered to incident solar radiation at 360 nm is used to calculate the attenuation factor since at this wavelength the absorption by ozone is very low and clouds and aerosols are assumed to be non-absorbing. This assumption may lead to errors in the estimated surface UV irradiances when absorbing aerosols are present in the atmosphere.

Chapter 3

Radiative Transfer Model

3.1 AccuRT

An accurate, efficient, and easy to use radiative transfer simulation tool, known as the Accurate Radiative Transfer (AccuRT), was used to compute the parameters used in models in this thesis. The AccuRT tool applies to coupled systems such as an atmosphere-water system or an atmosphere-snow-ice-water system. Each slab in a coupled system is taken to be a stratified medium in which the inherent optical properties (IOPs) can vary only along the direction of stratification, and no variation in IOPs is allowed in directions perpendicular to the direction of stratification [60, 92, 93].

The tool is used by researchers in remote sensing algorithm development, climate research, and other atmospheric and hydrological applications. The AccuRT tool is used to generate apparent optical properties (AOPs) such as upward and downward irradiances, scalar irradiances, and diffuse attenuation coefficients at any user-specified location in the coupled system for user-specified IOPs. Radiances in user-specified location and direction can also be computed with the tool [60, 92, 93].

The optical properties of a medium can be categorized as inherent or apparent. An IOP depends only on the medium itself, and not on the ambient light field within the medium. An AOP depends also on the illumination, i.e., on light propagating in particular directions inside and outside the medium [94].

3.2 Light and Matter

Light is part of the electromagnetic spectrum, which ranges from gamma rays to radio waves. The solar spectrum is mainly constituted of UV, visible, and infrared waves (e.g., see Fig. 2.3). The visible (400 – 700 nm) is the part of the solar spectrum which is detectable by the human eye. Electromagnetic radiation is described as a stream of photons. Photons are massless particles travelling with wavelike properties at the speed of light [95]. The detection of light by optical instruments is a way of measuring the properties of the atmosphere. By studying solar radiation at the surface of the Earth, after interaction with matter (particles and molecules) in the atmosphere, we can study the properties and composition of the atmosphere. The interaction of light with matter gives rise to various optical phenomena which helps us to understand matter and light itself.

Light interacts with matter through three different ways, i.e., emission, absorption, and scattering. Given a monochromatic ray of light, emission converts the internal energy of matter to radiative energy whereas absorption converts radiative energy into internal energy. Scattering is a double conversion process where radiative energy is absorbed by matter and then radiated. Therefore, the radiated field is modified in frequency, direction of propagation, and polarization relative to the absorbed field [60].

Matter is composed of discrete electric charges, i.e., electrons and protons. When an obstacle e.g., a single electron, an atom or molecule, a solid or liquid particle, is illuminated by an electromagnetic wave, the electric charges in the particle are set into oscillatory motion by the electric field of the incident wave. When electric charges are accelerated, they radiate electromagnetic energy in all directions. And it is this secondary radiation that is called the radiation scattered by the obstacle or particle [3]. Similarly, the incident electromagnetic energy may be transformed into other forms of energy (e.g., thermal energy), through absorption. All matter scatter light except the vacuum, and many phenomena which are not usually referred to as scattering phenomena are resulting from scattering. Examples may include diffuse reflection by rough surfaces, diffraction by slits, grating, edges, and specular reflection and refraction at optically smooth interfaces [3].

Manifestations of scattering of light can include, but not limited to; the blue sky, red sky at sunset, white light from clouds, scattering from surfaces, etc. The scattering of light by particles or molecules which are much smaller than the wavelength of incident light is called Rayleigh scattering. Rayleigh scattering is inversely proportional to the fourth power of wavelength of the scattered light. The Rayleigh scattering is the reason for the blue daytime sky as blue light is more scattered than the red, green, yellow or orange light. The red sunset is also due to Rayleigh scattering, but here the scattered light has to travel a long distance before reaching the observer and in the process the shorter wavelengths are scattered away from the observer and hence the red, yellow or orange sky at sunrise and sunset. During a lunar eclipse when the Moon passes

Figure 3.1: The blood Moon during total lunar eclipse. The picture is reprinted from MrEclipse.com [96].

through the shadow of the Earth, the Moon often has a vibrant red-orange color, as shown in Fig. 3.1. This striking color is due to the Rayleigh scattering of light by

particles and molecules in the Earth's atmosphere. Just like at sunrise or sunset, the shorter wavelengths of the visible light (blue and violet) are scattered the most, with the longer wavelengths (red and orange) remaining. The amount of aerosols present in the atmosphere also influence the color of the moon during lunar eclipse.

The scattering of light by particles or molecules larger than the wavelength of the incident light is called Mie scattering. Mie scattering is not strongly wavelength dependent and light is scattered more in the forward direction. It is the reason for white color of clouds as all light colors are scattered equally.

The absorption coefficient $a(\lambda)$ and the scattering coefficient $b(\lambda)$ are important IOPs, defined as [60]

$$a(z) = \frac{1}{I_i}\left(\frac{dI_a}{dz}\right) \qquad \left[\mathrm{m}^{-1}\right] \tag{3.1}$$

$$b(z) = \frac{1}{I_i}\left(\frac{dI_b}{dz}\right) \qquad \left[\mathrm{m}^{-1}\right], \tag{3.2}$$

where I_i is the incident radiance entering a volume element $dV = dAdz$ of the medium of cross section area dA and thickness dz, and $dI_a > 0$ and $dI_b > 0$ are respectively the radiances that are absorbed and scattered in all directions as the light propagates the distance dz.

The angular distribution of the scattered light is given in terms of the volume scattering function b_v, defined as [60]

$$b_v(z,\hat{\Omega}',\hat{\Omega}) = \frac{1}{I_i}\frac{d^2 I_b}{dz d\omega} = \frac{1}{I_i}\frac{d}{dz}\left(\frac{dI_b}{d\omega}\right) \qquad \left[\mathrm{m}^{-1}\mathrm{sr}^{-1}\right], \tag{3.3}$$

where $\hat{\Omega}'$ and $\hat{\Omega}$ are unit vectors, and $d^2 I_b$ is the radiance scattered from an incident direction $\hat{\Omega}'$ into a cone of solid angle $d\omega$ around the direction $\hat{\Omega}$ as light propagates the distance dz along the direction $\hat{\Omega}'$. The plane spanned by $\hat{\Omega}'$ and $\hat{\Omega}$ is called the scattering plane, and the scattering angle Θ is given by $\cos\Theta = \hat{\Omega}' \cdot \hat{\Omega}$. Integration of Eq. (3.3) over all scattering directions yields

$$\begin{aligned} b(z) &= \frac{1}{I_i}\frac{d}{dz}\int_{4\pi}\left(\frac{dI_b}{d\omega}\right)d\omega = \frac{1}{I_i}\left(\frac{dI_b}{dz}\right) \\ &= \int_{4\pi} b_v(z,\hat{\Omega}',\hat{\Omega})d\omega = \int_0^{2\pi}\int_0^{\pi} b_v(z,\cos\Theta,\phi)\sin\Theta d\Theta d\phi, \end{aligned} \tag{3.4}$$

where Θ and ϕ are respectively the polar angle and the azimuth angle in a spherical coordinate system in which the polar axis is along $\hat{\Omega}'$. A normalized volume scattering function, denoted by $p(z,\cos\Theta)$ and referred to as the scattering phase function, may be defined as follows

$$p(z,\cos\Theta) = 4\pi\frac{b_v(z,\cos\Theta)}{\int_{4\pi} b_v(z,\cos\Theta)d\omega} = \frac{b_v(z,\cos\Theta)}{\frac{1}{2}\int_{-1}^{1} b_v(z,\cos\Theta)d(\cos\Theta)} \tag{3.5}$$

Given a scattering event, $p(z,\cos\Theta)d\omega/4\pi$ is the probability that a light beam travelling in the direction $\hat{\Omega}'$ is scattered into a cone of solid angle $d\omega$ around the direction

$\hat{\Omega}'$. The scattering phase function $p(z,\cos\Theta)$ is a dimensionless parameter and it describes the angular distribution of the scattered radiation so that

$$\frac{1}{4\pi}\int_{\Omega} p(z,\cos\Theta)d\omega = \frac{1}{4\pi}\int_0^{2\pi}\int_0^{\pi} p(z,\cos\Theta)sin\theta d\theta d\phi = 1. \tag{3.6}$$

An asymmetry factor g is defined as

$$g = \frac{1}{2}\int_{-1}^{1} p(z,\cos\Theta)cos\Theta d(cos\Theta). \tag{3.7}$$

The asymmetry factor g can have different values for different types of scattering, i.e.

$g = 0$ For isotropic scattering
$g > 0$ Forward scattering
$g < 0$ Backward scattering.

A single parameter scattering phase function proposed by Henyey and Greenstein [97], can be written as

$$p(\cos\Theta) = \frac{1-g^2}{(1+g^2-2g\cos\Theta)^{3/2}}, \tag{3.8}$$

where g is the asymmetry factor. Although the Henyey and Greenstein scattering phase fuction has no physical basis, it is a useful tool for describing highly scattering media such as sea ice or skin for which the actual scattering phase functions are not known.

In the Rayleigh scattering limit, i.e. the size z of the scatterers is much smaller than the wavelength of light, the Rayleigh scattering phase function is used to describe the angular distribution of the scattered light. Rayleigh scattering phase function is given by

$$p(\cos\Theta) = \frac{3}{3+d}(1+d\cos^2\Theta) \tag{3.9}$$

where d is the depolarization factor [98]. The Rayleigh scattering phase function is symmetric about $\Theta = 90^\circ$, and thus $g = 0$.

3.3 Radiative Transfer Equation

The radiative transfer equation (RTE) is used to calculate the solar irradiance at any given location in a coupled system. The solar UV radiation penetrating the atmospheric layers consists of a direct and diffuse components. The direct component I_s is part of the incoming solar radiation field which has been attenuated by particles and molecules through extinction (i.e., absorption and scattering) during its propagation through the atmosphere. The diffuse component is the part of the solar radiation that has been scattered at least once by particles and molecules in the atmosphere [60]. The RTE can be set up according to the law of energy conservation, i.e., the first law of thermodynamics. The RTE consists of three main parts, i.e., the streaming term, which represents the directional flow of radiation, an extinction term (direct or solar component), which describes the loss of radiation due to absorption and scattering, and the source function, which contains all the sources of radiation.

We consider a coupled system consisting of two adjacent layers in the atmosphere separated by a plane, horizontal interface across which the refractive index changes abruptly from a value m_1 in layer 1 to a value m_2 in layer 2. If the IOPs are allowed to vary only in the vertical direction z, where z increases upward, the corresponding optical depth $\tau(z)$ is defined by [60]

$$\tau(z) = \int_z^\infty \big(a(z') + b(z')\big)\, dz' \tag{3.10}$$

where the absorption and scattering coefficients a and b are defined in Eqs. (3.1) and (3.2). Note that the optical depth is defined to increase downward from $\tau(z = \infty) = 0$ at the top of the atmosphere.

The downward direct solar component as described by the extinction law is given by [60]

$$I_s(\tau, \mu, \phi) = F^s \delta(\hat{\Omega} - \hat{\Omega}_0) e^{-\tau/\mu_0} = F^s \delta(\mu - \mu_0)(\phi - \phi_0) e^{-\tau/\mu_0}, \tag{3.11}$$

where F^s is the extraterrestrial solar irradiance at the top of the atmosphere in the direction (θ_0, ϕ_0), $\hat{\Omega}_0$ and $\hat{\Omega}$ are respectively denoting the incoming and outgoing beam directions, $\mu_0 = \cos\theta_0$, $\mu = \cos\theta$, θ is the polar angle, and ϕ is the azimuth angle.

If the two layers are assumed to be in local thermodynamic equilibrium (LTE), thus emitting radiation according to the local temperature $T(\tau(z))$, the transfer of the diffuse radiance $I(\tau, \mu, \phi)$ through a plane-parallel, absorbing, and scattering, vertically inhomogeneous medium is described by the RTE [60]

$$\begin{aligned} \mu \frac{dI(\tau, \mu, \phi)}{d\tau} = I(\tau, \mu, \phi) - \frac{\alpha(\tau)}{4\pi} \int_0^{2\pi} d\phi' \int_{-1}^{1} p(\tau, \mu', \phi'; \mu, \phi) I(\tau, \mu', \phi') d\mu' \\ -(1 - \alpha(\tau)) B(\tau) - S^*(\tau, \mu', \phi'), \end{aligned} \tag{3.12}$$

where $\alpha(\tau) = b(\tau)/\left(a(\tau) + b(\tau)\right)$ is the single-scattering albedo, $p(\tau, \mu', \phi'; \mu, \phi)$ is the scattering phase function defined by Eq. (3.5), and $B(\tau)$ is the thermal radiation field given by the Planck function. The differential vertical optical depth is derived from Eq. (3.10)

$$d\tau(z) = -\left(a(\tau) + b(\tau)\right) dz, \tag{3.13}$$

where the minus sign indicates that τ increases in the downward direction, whereas z increases in the upward direction, as noted above. The scattering angle Θ and the polar and azimuth angles are related by

$$\hat{\Theta}' \cdot \hat{\Theta} = \cos\theta \cos\theta' + \sin\theta \sin\theta' \cos(\phi' - \phi). \tag{3.14}$$

By definition, $\theta = 180^\circ$ is directed toward nadir and $\theta = 0^\circ$ toward zenith. Thus, $\mu = \cos\theta$ varies in the range [-1, 1] (i.e., from nadir to zenith). For cases of oblique illumination of the system, $\phi = 180^\circ$ is defined to be the azimuth angle of the incident light.

The single-scattering source term $S^*(\tau, \mu, \phi)$ in Eq. (3.12) in layer 1 (with complex refractive index $m_1 = n_1 + in_1$) is different from that in the lower layer (layer 2 , with complex refractive index $m_2 = n_2 + in_2$). In layer 1 it is given by

$$\begin{aligned} S_1^*(\tau, \mu, \phi) = \frac{\alpha(\tau)}{4\pi} p(\tau, -\mu_0, \phi_0; \mu, \phi) F^s e^{-\tau/\mu_0} \\ + \frac{\alpha(\tau)}{4\pi} \rho_F(-\mu_0; m_1, m_2) p(\tau, \mu_0, \phi_0; \mu, \phi) F^s e^{-(2\tau_1 - \tau)/\mu_0}, \end{aligned} \tag{3.15}$$

where τ_1 is the vertical optical depth of layer$_1$, $\rho_F(-\mu_0,;m_1,m_2)$ is the Fresnel reflectance at the layer 1 – layer 2 interface. The first term on the right-hand side of Eq. (3.15) is due to first order scattering of the attenuated incident beam of irradiance F^s, while the second term is due to first order scattering of the attenuated incident beam that is reflected at the layer 1 – layer 2 interface. In layer 2 the single-scattering source term consists of the attenuated incident beam that is refracted through the interface, i.e.,

$$\begin{aligned} S_2^*(\tau,\mu,\phi) &= \frac{\alpha(\tau)}{4\pi}\frac{\mu_0}{\mu_{0_n}}T_F(-\mu_0,;m_1,m_2) \\ &\times p(\tau,-\mu_{0_n},\phi_0;\mu,\phi)e^{-\tau_1/\mu_0}e^{-(\tau-\tau_a)/\mu_{0_n}}, \end{aligned} \tag{3.16}$$

where $T_F(-\mu_0;m_1,m_2)$ is the Fresnel transmittance through the interface, and μ_{0_n} is the cosine of the polar angle θ_{0_n} in layer 2, which is related to $\theta_0 = \arccos\mu_0$ by Snell's law.

3.3.1 Solutions to the Radiative Transfer Equation

As a beam of radiation propagates through a medium, it is affected by absorption, emission, and scattering processes. It loses energy through absorption, generates energy through emissions, and redistributes energy through scattering. The RTE is used as a mathematical description of these interactions processes. From the RTE (Eq. (3.12)) we can define a source function $S(\tau,\hat{\Omega})$ as

$$S(\tau,\hat{\Omega}) = (1-\alpha(\tau))B(\tau) + \frac{\alpha(\tau)}{4\pi}\int_{4\pi} d\omega' p(\tau,\hat{\Omega}',\hat{\Omega})I(\tau,\hat{\Omega}'), \tag{3.17}$$

where at the LTE it coincides with the Planck function $B(\tau)$ at the local temperature.

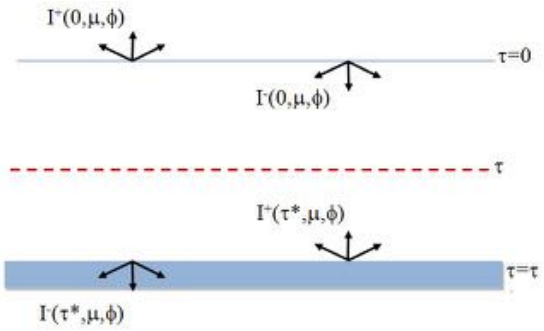

Figure 3.2: Half-range intensities in a plane-parallel atmosphere. The optical depth is measured downwards from the top to the bottom of the medium.

3.3.2 Classical Solution of the RTE

If we neglected the time dependent effects and the presence of the potential gradient on the radiation field in a plane-parallel atmosphere, the RTE may be written as

$$\mu\frac{dI(\tau,\mu,\phi)}{d\tau} = I(\tau,\mu,\phi) + S(\tau,\mu,\phi). \tag{3.18}$$

Equation (3.18) is a linear differential equation, and this means that a formal solution exists for the radiation field in terms of the source function $S(\tau,\mu)$. The complete solution may be written as the sum of the solution to the homogeneous equation and any particular solution. The homogeneous equation is found by dropping the source function in Eq. (3.18) and has the following solution

$$I_H(\tau,\mu,\phi) = h_1 e^{-\tau/\mu} + h_2 e^{\tau/\mu}. \tag{3.19}$$

If we choose a particular solution as

$$I_P(\tau,\mu,\phi) = y(\tau) e^{\tau/\mu}, \tag{3.20}$$

and a substitution of Eqs. (3.19) and (3.20) into the RTE in Eq. (3.18), gives

$$\begin{aligned} h_1 &= 0 \\ y'(\tau) &= \frac{-S(\tau,\mu,\phi)e^{-\tau/\mu}}{\mu}. \end{aligned}$$

Then the general classical solution for a plane-parallel atmosphere may be written as

$$I(\tau,\mu,\phi) = h_2 e^{\tau/\mu} - \int S(\tau',\mu,\phi) e^{-(\tau'-\tau)/\mu} \frac{d\tau'}{\mu}. \tag{3.21}$$

In terms of half-range intensities in Fig. 3.2, the general classical solution can be written as

$$\begin{aligned} I^-(\tau,\mu,\phi) &= I^-(0,\mu,\phi)e^{-\tau/\mu} + \int_0^\tau \frac{d\tau'}{\mu} S(\tau',\mu,\phi) e^{-(\tau-\tau')/\mu} \\ I^+(\tau,\mu,\phi) &= I^+(\tau^*,\mu,\phi)e^{(\tau-\tau^*)/\mu} + \int_\tau^{\tau^*} \frac{d\tau'}{\mu} S(\tau',\mu,\phi) e^{(\tau-\tau')/\mu}. \end{aligned} \tag{3.22}$$

3.3.3 Solution without Scattering

In the limit of no scattering, the propagating radiation is only affected by absorption and emission processes. If we consider a plane-parallel medium in Fig. 3.2, and take the medium properties to vary only in the vertical direction due to the gravity imposed stratification [60], the half-range intensities can be defined as

$$\begin{aligned} I^+(\tau,\mu,\phi) &:= I(\tau,\mu \le 0,\phi) \\ I^-(\tau,\mu,\phi) &:= I(\tau,\mu > 0,\phi). \end{aligned} \tag{3.23}$$

Using Eq. (3.12) and assuming there is no scattering, the RTE for half-range intensities can be written as

$$\mu \frac{dI^+(\tau,\mu,\phi)}{d\tau} = I^+(\tau,\mu,\phi) - B(\tau) \tag{3.24}$$

$$-\mu \frac{dI^-(\tau,\mu,\phi)}{d\tau} = I^-(\tau,\mu,\phi) - B(\tau). \tag{3.25}$$

The minus sign on the LHS of Eq. (3.25) is due to the absorption optical depth, which is measured downwards from the top of the medium. Using an integrating factor of $e^{\tau/\mu}$, Eq. (3.25) is written as a perfect differential equation

$$\frac{d}{d\tau}\left(I^- e^{\tau/\mu}\right) = \left(\frac{dI^-}{d\tau} + \frac{1}{\mu} I^-\right) e^{\tau/\mu} = \frac{B(\tau)}{\mu} e^{\tau/\mu}. \tag{3.26}$$

We can now integrate Eq. (3.26) along the vertical from the top at $\tau = 0$ downwards to τ (inside the medium)

$$\begin{aligned}\int_0^\tau d\tau' \frac{d}{d\tau'}\left(I^- e^{\tau'/\mu}\right) &= I^-(\tau,\mu,\phi)e^{\tau/\mu} - I^-(0,\mu,\phi) \\ &= \int_0^\tau \frac{d\tau'}{\mu} e^{\tau'/\mu} B(\tau').\end{aligned}$$

And solving for $I^-(\tau,\mu,\phi)$, we get the intensity at any point τ inside the atmosphere

$$I^-(\tau,\mu,\phi) = I^-(0,\mu,\phi)e^{-\tau/\mu} + \int_0^\tau \frac{d\tau'}{\mu} B(\tau') e^{-(\tau-\tau')/\mu} \tag{3.27}$$

Similarly using an integrating of $e^{-\tau/\mu}$, the upper half-range intensity can be written as a perfect differential equation. And integrating from the bottom of the medium to a point τ inside the medium, we obtain

$$\begin{aligned}\int_{\tau^*}^\tau d\tau' \frac{d}{d\tau'}\left(I^+ e^{-\tau'/\mu}\right) &= I^+(\tau,\mu,\phi)e^{-\tau/\mu} - I^+(\tau^*,\mu,\phi)e^{-\tau^*/\mu} \\ &= -\int_{\tau^*}^\tau \frac{d\tau'}{\mu} e^{-\tau'/\mu} B(\tau') = \int_\tau^{\tau^*} \frac{d\tau'}{\mu} e^{-\tau'/\mu} B(\tau').\end{aligned}$$

And solving for $I^+(\tau,\mu,\phi)$ the intensity at an interior point τ becomes

$$I^+(\tau,\mu,\phi) = I^+(\tau^*,\mu,\phi)e^{-(\tau^*-\tau)/\mu} + \int_\tau^{\tau^*} \frac{d\tau'}{\mu} e^{-(\tau'-\tau)/\mu} B(\tau'). \tag{3.28}$$

In the limit $\mu \to 0$ and since $B(\tau)$ is constant in Eq. (3.27) and (3.28), we have

$$I^\pm(\tau,\mu=0,\phi) = B(\tau). \tag{3.29}$$

3.3.4 Solution with Scattering and Emission

If scattering can not be neglected, the extinction (scattering and absorption) optical depth becomes an independent variable, and the RTE is given as [60]

$$\mu \frac{dI(\tau,\hat{\Omega})}{d\tau} = I(\tau,\hat{\Omega}) + S(\tau,\hat{\Omega}). \tag{3.30}$$

For a plane-parallel medium, the solution to Eq. (3.30) is given by Eq. (3.27), (3.28), and (3.29) where we replace the Planck function with the source function

$$I^-(\tau,\mu,\phi) = I^-(0,\mu,\phi)e^{-\tau/\mu} + \int_0^\tau \frac{d\tau'}{\mu} S(\tau',\mu,\phi) e^{-(\tau-\tau')/\mu} \tag{3.31}$$

$$I^+(\tau,\mu,\phi) = I^+(\tau^*,\mu,\phi)e^{-(\tau^*-\tau)/\mu} + \int_\tau^{\tau^*} \frac{d\tau'}{\mu} S(\tau',\mu,\phi)e^{-(\tau'-\tau)/\mu}. \tag{3.32}$$

$$I^\pm(\tau,\mu=0,\phi) = S(\tau,\mu=0,\phi). \tag{3.33}$$

The source function S can easily be derived from Eq. (3.17)

$$\begin{aligned} S(\tau,\mu,\phi) = (1-\alpha(\tau))B(\tau) + \frac{\alpha(\tau)}{4\pi}\int_0^{2\pi} d\phi' \int_0^1 d\mu' p(\mu',\phi';\mu,\phi) I^+(\tau,\mu',\phi') \\ + \frac{\alpha(\tau)}{4\pi}\int_0^{2\pi} d\phi' \int_0^1 d\mu' p(-\mu',\phi';\mu,\phi) I^-(\tau,\mu',\phi'). \end{aligned} \tag{3.34}$$

3.3.5 Discrete-ordinate Solution of the RTE

The scattering phase function in Eq. (3.12) may be expanded in a finite series of $2N$ Legendre polynomials, and by applying the Addition theorem for spherical harmonics, one obtains [60]

$$p(\cos\Theta) = p(\mu',\phi';\mu,\phi) = \sum_{m=0}^{2N-1} (2-\delta_{0,m}) p^m(\mu',\mu)\cos m(\phi'-\phi). \tag{3.35}$$

Here $\delta_{0,m}$ is the Kronecker delta function, where $\delta_{0,m} = 1$ for $m = 0$ and $\delta_{0,m} = 0$ otherwise. And

$$p^m(\mu',\mu) = \sum_{l=m}^{2N-1} (2l+1)\chi_l \Lambda_l^m(\mu')\Lambda_l^m(\mu), \tag{3.36}$$

where the expansion coefficient χ_l is given by

$$\chi_l = \frac{1}{2}\int_{-1}^{1} d(\cos\Theta) P_l(\cos\Theta) p(\cos\Theta),$$

and Λ_l^m is defined as

$$\Lambda_l^m := \sqrt{\frac{(l-m)!}{(l+m)!}} P_l^m(\mu),$$

where P_l^m is the Legendre polynomial of order m.

The radiance intensities can be expanded in a similar way to obtain

$$I(\tau,\mu,\phi) = \sum_{m=0}^{2N-1} I^m(\tau,\mu)\cos m(\phi-\phi_0), \tag{3.37}$$

where ϕ_0 is the azimuth angle of the incident light. It can also be shown that each of the Fourier components satisfies the following RTE [60]

$$\begin{aligned} \mu\frac{dI^m(\tau,\mu)}{d\tau} = I^m(\tau,\mu) - \frac{\alpha(\tau)}{2}\int_{-1}^{1} d\mu' p^m(\tau,\mu',\mu) I^m(\tau,\mu') \\ - \chi_0^m(\tau,\mu)e^{-\tau/\mu_0} - (1-\alpha)B(\tau)\delta_{0,m}. \end{aligned} \tag{3.38}$$

where $m = 0,1,2,...,2N-1$ and $p^m(\tau,\mu',\mu)$ is given by Eq. (3.36).

Thomas and Stamnes [60] gives the complete homogeneous solution of Eq. (3.38) for the plane-parallel atmosphere as

$$I^{\pm}(\tau,\mu_i) = \sum_{j=1}^{1} \left(C_{-j} \cdot g_{-j}(\pm\mu_i) e^{k_j \tau} + C_j \cdot g_j(\pm\mu_i) e^{-k_j \tau} \right), \tag{3.39}$$

where $i = 1,2,3,...,N$, g_j and k_j are eigenvectors and eigenvalues, and C_j and C_{-j} are integration constants.

Chapter 4

Introduction to Papers

Paper I: *T. Ssenyonga, D. Muyimbwa, W. Okullo, Y. -C. Chen, Ø. Frette, B. Hamre, A. Steigen, A. Dahlback, and J. J. Stamnes, Aerosols in coastal and inland areas in the equatorial African belt. Appl. Opt.* ***53****, 2964–2973, 2014.*

Aerosols affect the climate directly through absorption and reflection of sunlight back to space and indirectly by acting as cloud condensation nuclei. This paper is based on more than three decades of satellite data (1979–1994 and 1996–2012) from total ozone mapping spectrometer (TOMS) and ozone monitoring instrument (OMI), which have provided measurements of backscattered radiances in the wavelength range from 331 to 380 nm. These data have been used to determine the aerosol climatology and to investigate the influence of the aerosol index (AI) on the ultraviolet index (UVI) in coastal land areas in Serrekunda (13.28° N, 16.34° W), The Gambia, and Dar-es-Salaam (6.8° S, 39.26° E), Tanzania, as well as in inland areas in Kampala (0.19° N, 32.34° E), Uganda. Heavy aerosol loadings were found to occur in the dry seasons at all three locations. To reduce the influence of clouds, we disregarded TOMS and OMI data for days during which the UV reflectivity was larger than 9% and investigated the correlation of the AI with the UVI for the remaining days at the three locations. We found a high correlation coefficient of 0.82 for Serrekunda, but poor correlation for Kampala and Dar-es-Salaam. The average AI for Serrekunda was found to be about three times higher than that for Kampala or Dar-es-Salaam, and a positive trend was found for the AI in Kampala and Dar-es-Salaam, whereas a negative trend was found for the AI in Serrekunda.

My contribution was in data analysis and writing of the paper.

Paper II: *D. Muyimbwa, A. Dahlback, T. Ssenyonga, Y. -C. Chen, J. J. Stamnes, Ø. Frette, and B. Hamre, Validation of ozone monitoring instrument ultraviolet index against ground-based UV index in Kampala, Uganda. Appl. Opt.* ***54****, 8537–8545, 2015.*

The Ozone Monitoring Instrument (OMI) overpass solar ultraviolet (UV) indices have been validated against the ground-based UV indices derived from Norwegian Institute for Air Research UV measurements in Kampala (0.31° N, 32.58° E, 1200 m), Uganda for the period between 2005 and 2014. An excessive use of old cars, which would imply a high loading of absorbing aerosols, could cause the OMI retrieval algorithm to

overestimate the surface UV irradiances. The UV index values were found to follow a seasonal pattern with maximum values in March and October. Under all-sky conditions, the OMI retrieval algorithm was found to overestimate the UV index values with a mean bias of about 28%. When only days with radiation modification factor (RMF) greater or equal to 65%, 70%, 75%, and 80% were considered, the mean bias between ground-based and OMI overpass UV index values was reduced to 8%, 5%, 3%, and 1%, respectively. The overestimation of the UV index by the OMI retrieval algorithm was found to be mainly due to clouds and aerosols.

I contributed in data analysis and writing of the paper with help from all the co-authors.

Paper III: *D. Muyimbwa, Ø. Frette, J. J. Stamnes, T. Ssenyonga, Y. -C. Chen, and B. Hamre, Aerosol optical properties and precipitable water vapor column in the atmosphere of Norway. Appl. Opt.* ***54****, 1505–1514, 2015.*

Between February 2012 and April 2014, we measured and analyzed direct solar radiances at a ground-based station in Bergen, Norway. We discovered that the spectral aerosol optical thickness (AOT) and precipitable water vapor column (PWVC) retrieved from these measurements have a seasonal variation with highest values in summer and lowest values in winter. The highest value of the monthly median AOT at 440 nm of about 0.16 was measured in July and the lowest of about 0.04 was measured in December. The highest value of the monthly median PWVC of about 2.0 cm was measured in July and the lowest of about 0.4 cm was measured in December. We derived Ångström exponents that were used to deduce aerosol particle size distributions. We found that coarse-mode aerosol particles dominated most of the time during the measurement period, but fine-mode aerosol particles dominated during the winter seasons. The derived Ångström exponent values suggested that aerosols containing sea salt could have been dominating at this station during the measurement period.

I participated in the measurement process, analysed the data and wrote the paper with help from all the co-authors.

Paper IV: *Y. -C. Chen, B. Hamre, Ø. Frette, D. Muyimbwa, S. Blindheim, K. Stebel, P. Sobolewski, C. Toledano, and J. J. Stamnes, Aerosol optical properties in Northern Norway and Svalbard. Accepted for publication in Appl. Opt.*

We present comparisons between estimates of the aerosol optical thickness and the Ångström exponent in Northern Norway and Svalbard based on data from AERONET (Aerosol Robotic Network) stations at Andenes (69.28° N, 16.01° E, 379 m altitude) and Hornsund (77.00° N, 15.56° E, 10 m altitude) for the period 2008–2011. The four-year annual mean values for the aerosol optical thickness at 500 nm $\tau(500)$ at Andenes and Hornsund both were 0.10. At Hornsund, there was less variation of the monthly mean value of $\tau(500)$ than at Andenes. The annual mean values of the Ångström exponent α at Andenes and Hornsund were 1.25 and 1.37, respectively. At Andenes and Hornsund α was found to be larger than 1.1 in 64% and 86% of the observations, respectively, indicating that fine-mode particles were dominating at both sites. Both sites

had a similar seasonal variation of the aerosol size distribution although one site is in an arctic area while the other site is in a sub-arctic area.

I contributed in data analysis.

Chapter 5

Conclusion and Outlook

The main focus of this thesis has been to study aerosols and solar UV radiation by using both ground-based and satellite measurements. During this period we have conducted four studies on aerosols and solar UV radiation. The aerosol optical properties were measured from a ground-based site in Bergen, Norway, for the period between 2012 and 2014. The results from these measurements were presented in Paper III, where we found that both AOT and PWVC follow a seasonal pattern with maximum values in summer and minimum values in winter. The Ångström exponent value was used to deduce particle size distribution which led us to conclude that coarse-mode aerosol particles were dominating most of the time during the measurement period, but fine-mode aerosol particles were found to dominate during winter seasons.

The city of Bergen where our measurement site was located, is surrounded by mountains and at such a location, the city is prone to temperature inversions. We were interested to see how anthropogenic aerosols especially those from combustion of fossil fuel by cars and boats influence the atmosphere during temperature inversions. Unfortunately, the weather conditions were not always good for radiance measurements whenever there was a temperature inversion. Radiance measurements require that the sun is above the horizon and the sky is free of clouds. But during temperature inversion it was either foggy or the sun was below the horizon, making it impossible to make radiance measurements.

However, there was a temperature inversion on 20th January, 2013 that lasted for several hours between 01:00 and 14:00 (UTC) and it happened on a clear-sky day. The weather station on Mount Ulriken measured an average temperature of about 4° warmer than the temperature measured by the weather station at Florida. Mount Ulriken is about 643 m high and Florida is about 12 m above sea-level. These two weather stations are run and managed by the Department of Geophysics, University of Bergen.

Although the measured AOT values were small, the Ångström exponent value was about 2. An Ångström exponent value larger than 1 would imply a great contribution of fine-mode aerosol particles such as smoke and vehicle exhausts to the total atmospheric extinction. This means that even if the AOT values were small, the atmospheric extinction was greatly influenced by smoke and urban hazy. This could lead to serious health implication as polluted air is trapped close to the surface. The temperature inversion prevents the polluted air to escape and mix with the air in higher atmospheric layers. This is because the cold air close to the surface is denser than the warm air above in the atmosphere and this will continue until the temperature warms up.

In another study, we analysed aerosols data from AERONET sites at Hornsund, Svalbard and at Andenes in northern Norway. The site at Hornsund is in the Arctic whereas Andenes is in the sub-Arctic. It was found that both sites had the same annual mean AOT values and a similar aerosol size distribution in the summer. As expected, we found that measurements at Andenes are more influenced by the anthropogenic aerosols or urban haze than those from Hornsund. This was due to their locations since Andenes is closer to industrialised Europe than Hornsund, which is in the Arctic.

The measurements from Andenes were also compared with those from Bergen where we found some similarities in the AOT values and differences in the PWVC values. We expected some similarities in the aerosol types since both sites experience maritime environment. But Bergen being a larger city than Andenes and in the south, it experiences more urban haze and this may affect the AOT and the PWVC values.

In a study conducted on the African belt, the aerosol index (AI), which is a measure of the wavelength-dependent absorption by aerosols of the back-scattered radiance coming from Rayleigh scattering by molecules that are located below the aerosol layer, was analysed using satellite measurements from TOMS and OMI instruments. The AI has a positive value for UV absorbing aerosols and a negative value for non absorbing aerosols. The influence of AI on the UV index from three locations on the African belt was presented in Paper I. A high correlation coefficient between the AI and the UV index of about 8.2 was found for Serrekunda, but a poor correlation for both Kampala and Dar-es-Salaam. The average AI for Serrekunda was three times higher than that for Kampala or Dar-es-Salaam. The trends for the annual average AI values were positive for both Kampala and Dar-es-Salaam, but negative for Serrekunda.

The final study was conducted to validate satellite measurements using long term ground-based UV measurements. The solar UV radiation measurements from Kampala, Uganda, were analysed and compared with similar measurements from the OMI instrument. We found the OMI retrieval algorithm to overestimate the UV index values with a mean bias of about 28% under all-sky conditions. But under the clear-sky, the bias was reduced to as low as 1%. The annual mean local noon TOC and UV index values were observed to be remarkably stable over the observation period (see Fig. 5.1). We noticed a 22% average reduction of the UV index values due to aerosols and clouds, by comparing measured values to calculated clear-sky UV index values using TOC values inferred from OMI measurements (see Fig. 5.2). In future, such studies may be broadened to give more information on aerosols' influence on solar radiation by installing sun-photometers along side UV irradiance meters.

In addition to providing instrument validation and method development, this thesis has shown that ground-based and satellite remote sensing of atmospheric aerosols and ultraviolet solar radiation can reveal important properties about the environment that can possibly influence human health and well-being. It is therefore important that such measurements and analysis will continue on a global scale in the future.

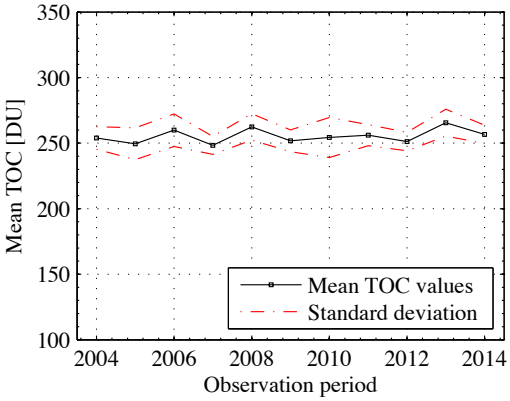

Figure 5.1: The annual average TOC values inferred from OMI measurements at a site in Kampala, Uganda.

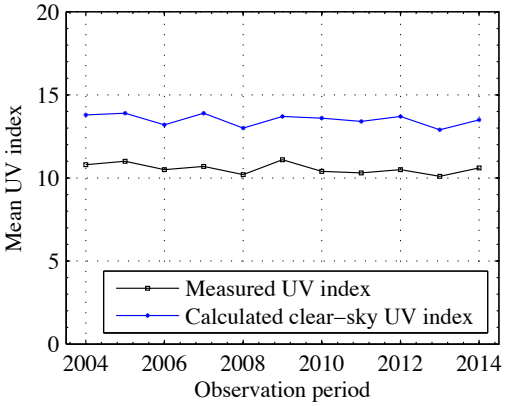

Figure 5.2: The annual average values of the measured UV index at local solar noon and the clear-sky UV index calculated using TOC values inferred from OMI measurements at a site in Kampala, Uganda.

Chapter 6

Scientific Results

Bibliography

[1] NASA Langley Research Center. Atmospheric Aerosols. http://www.nasa.gov/centers/langley/news/factsheets/Aerosols.html, 2015. 1.1

[2] M. Kanakidou, J. H. Seinfeld, S. N. Pandis, I. Barnes, F. J. Dentener, M. C. Facchini, R. Van Dingenen, B. Ervens, A. Nenes, C. J. Nielsen, E. Swietlicki, J. P. Putaud, Y. Balkanski, S. Fuzzi, J. Horth, G. K. Moortgat, R. Winterhalter, C. E. L. Myhre, K. Tsigaridis, E. Vignati, E. G. Stephanou, and J. Wilson. Organic aerosol and global climate modelling: a review. *Atmos. Chem. Phys.*, 5:1053–1123, 2005. 1.1, 1.1.2

[3] C. F. Bohren and D. R. Huffman. *Absorption and scattering of light by small particles*. John Wiley & Sons, 2008. 1.1, 1.1.2, 3.2

[4] R. J. Charlson, S. E. Schwartz, J. M. Hales, R. D. Cess, Jr. J. A. COAKLEY, J. E. Hansen, and D. J. Hofmann. Climate forcing by anthropogenic aerosols. *Science*, 255:423–430, 1992. 1.1.1, 1.1.1

[5] Y. J. Kaufman, D. Tanré, L. A. Remer, E. F. Vermote, A. Chu, and B. N. Holben. Operational remote sensing of tropospheric aerosol over land from EOS moderate resolution imaging spectroradiometer. *J. Geophys. Res.*, 102:17051–17067, 1997. 1.1.1

[6] George Miller and Scott Spoolman. *Living in the environment: principles, connections, and solutions*. Cengage Learning, 2011. 1.1.1

[7] A. A. Kokhanovsky. *Aerosol optics: Light absorption and scattering by particles in the atmosphere*. Springer Science & Business Media, 2008. 1.1.1, 1.1.1, 1.1.1, 1.1.1, 1.1.1, 1.1.1, 1.1.1, 1.1.1

[8] Ulrich Pöschl. Atmospheric aerosols: composition, transformation, climate and health effects. *Angew. Chem. Int. Ed. Engl.*, 44:7520–7540, 2005. 1.1.1, 1.1.1

[9] Victor Hugo. What dust does. http://www.lastwordonnothing.com/2014/05/07/what-dust-does/, 2015. (document), 1.1

[10] M. Schulz, G. de Leeuw, and Y. Balkanski. Sea-salt aerosol source functions and emissions. In *Emissions of Atmospheric Trace Compounds*, pages 333–359. Springer, 2004. 1.1.1

[11] Z. Levin and W. R. Cotton. *Aerosol pollution impact on precipitation: A scientific review*. Springer Science & Business Media, 2008. 1.1.1

[12] I. N. Tang and H. R. Munkelwitz. Water activities, densities, and refractive indices of aqueous sulfates and sodium nitrate droplets of atmospheric importance. *J. Geophys. Res.*, 99:18801–18808, 1994. 1.1.1

[13] C. D. O'Dowd, M. C. Facchini, F. Cavalli, D. Ceburnis, M. Mircea, S. Decesari, S. Fuzzi, Y. J. Yoon, and J. P. Putaud. Biogenically driven organic contribution to marine aerosol. *Nature*, 431:676–680, 2004. 1.1.1

[14] J. S. Reid, H. H. Jonsson, M. H. Smith, and A. Smirnov. Evolution of the vertical profile and flux of large sea-salt particles in a coastal zone. *J. Geophys. Res.*, 106: 12039–12053, 2001. 1.1.1

[15] Y. Shinozuka, A. D. Clarke, S. G. Howell, V. N. Kapustin, and B. J. Huebert. Sea-salt vertical profiles over the Southern and tropical Pacific oceans: Microphysics, optical properties, spatial variability, and variations with wind speed. *J. Geophys. Res.*, 109(D24201), 2004. 1.1.1

[16] A. Goudie and N. J. Middleton. *Desert dust in the global system*. Springer Science & Business Media, 2006. 1.1.1

[17] N. M. Mahowald, S. Kloster, S. Engelstaedter, J. K. Moore, S. Mukhopadhyay, J. R. McConnell, S. Albani, S. C. Doney, A. Bhattacharya, M. A. J. Curran, M. G. Flanner, F. M. Hoffman, D. M. Lawrence, K. Lindsay, P. A. Mayewski, J. Neff, D. Rothenberg, E. Thomas, P. E. Thornton, and C. S. Zender. Observed 20th century desert dust variability: impact on climate and biogeochemistry. *Atmos. Chem. Phys.*, 10:10875–10893, 2010. 1.1.1

[18] I. Koren, Y. J. Kaufman, R. Washington, M. C. Todd, Y. Rudich, J. V. Martins, and D. Rosenfeld. The bodélé depression: a single spot in the sahara that provides most of the mineral dust to the amazon forest. *Environ. Res. Lett.*, 1:014005, 2006. 1.1.1

[19] H. Yu, M. Chin, T. Yuan, H. Bian, L. A. Remer, J. M. Prospero, A. Omar, D. Winker, Y. Yang, Y. Zhang, Z. Zhang, and C. Zhao. The fertilizing role of African dust in the Amazon rainforest: A first multiyear assessment based on data from Cloud-Aerosol Lidar and Infrared Pathfinder Satellite Observations. *Geophys. Res. Lett.*, 42:1984–1991, 2015. 1.1.1

[20] I. Tegen and A. A. Lacis. Modeling of particle size distribution and its influence on the radiative properties of mineral dust aerosol. *J. Geophys. Res.*, 101:19237–19244, 1996. 1.1.1

[21] M. Hallquist, J. C. Wenger, U. Baltensperger, Y. Rudich, D. Simpson, M. Claeys, J. Dommen, N. M. Donahue, C. George, A. H. Goldstein, J. F. Hamilton, H. Herrmann, T. Hoffmann, Y. Iinuma, M. Jang, M. E. Jenkin, J. L. Jimenez, A. Kiendler-Scharr, W. Maenhaut, G. McFiggans, Th. F. Mentel, A. Monod, A. S. H. Prévôt, J. H. Seinfeld, J. D. Surratt, R. Szmigielski, and J. Wildt. The formation, properties and impact of secondary organic aerosol: current and emerging issues. *Atmos. Chem. Phys.*, 9:5155–5236, 2009. 1.1.1

[22] The Gaurdian Australia. New South Wales bushfires - "This is as bad as it gets". http://www.theguardian.com/world/2013/oct/17/bushfires-rage-in-nsw-as-emergency-warnings-issued-live-blog, 2013. (document), 1.2

[23] O. Möhler, P. J. DeMott, G. Vali, and Z. Levin. Microbiology and atmospheric processes: the role of biological particles in cloud physics. *Biogeosciences*, 4: 1059–1071, 2007. 1.1.1

[24] U. Pöschl, S. T. Martin, B. Sinha, Q. Chen, S. S. Gunthe, J. A. Huffman, S. Borrmann, D. K. Farmer, R. M. Garland, G. Helas, J. L. Jimenez, S. M. King, A. Manzi, E. Mikhailov, T. Pauliquevis, M. D. Petters, A. J. Prenni, P. Roldin, D. Rose, J. Schneider, H. Su, S. R. Zorn, P. Artaxo, and M. O. Andreae. Rainforest aerosols as biogenic nuclei of clouds and precipitation in the amazon. *Science*, 329:1513–1516, 2010.

[25] C. Pöhlker, K. T. Wiedemann, B. Sinha, M. Shiraiwa, S. S. Gunthe, M. Smith, H. Su, P. Artaxo, Q. Chen, Y. Cheng, W. Elbert, M. K. Gilles, A. L. D. Kilcoyne, R. C. Moffet, M. Weigand, S. T. Martin, U. Pöschl, and M. O. Andreae. Biogenic potassium salt particles as seeds for secondary organic aerosol in the amazon. *Science*, 337:1075–1078, 2012. 1.1.1

[26] R. E. Dales, S. Cakmak, S. Judek, T. Dann, F. Coates, J. R. Brook, and R. T. Burnett. The role of fungal spores in thunderstorm asthma. *CHEST*, 123:745–750, 2003. 1.1.1

[27] D. W. Denning, B. R. O'driscoll, C. M. Hogaboam, P. Bowyer, and R. M. Niven. The link between fungi and severe asthma: a summary of the evidence. *EUR. RESPIR. J.*, 27:615–626, 2006. 1.1.1

[28] H. A. Burge and W. R. Solomon. Sampling and analysis of biological aerosols. *Atmos. Environ.*, 21:451–456, 1987. 1.1.1

[29] J. S. Reid, R. Koppmann, T. F. Eck, and D. P. Eleuterio. A review of biomass burning emissions part ii: intensive physical properties of biomass burning particles. *Atmos. Chem. Phys.*, 5:799–825, 2005. 1.1.1

[30] N. Mahowald, D. S. Ward, S. Kloster, M. G. Flanner, C. L. Heald, N. G. Heavens, P. G. Hess, J. F. Lamarque, and P. Y. Chuang. Aerosol impacts on climate and biogeochemistry. *Ann. Rev. Environ. Resour.*, 36:45, 2011. 1.1.1

[31] J. F. Lamarque, T. C. Bond, V. Eyring, C. Granier, A. Heil, Z. Klimont, D. Lee, C. Liousse, A. Mieville, B. Owen, M. G. Schultz, D. Shindell, S. J. Smith, E. Stehfest, J. Van Aardenne, O. R. Cooper, M. Kainuma, N. Mahowald, J. R. McConnell, V. Naik, K. Riah, and D. P. van Vuuren. Historical (1850–2000) gridded anthropogenic and biomass burning emissions of reactive gases and aerosols: methodology and application. *Atmos. Chem. Phys.*, 10:7017–7039, 2010. 1.1.1

[32] J. Hansen and L. Nazarenko. Soot climate forcing via snow and ice albedos. *Proc. Natl. Acad. Sci. U.S.A.*, 101:423–428, 2004. 1.1.1

[33] M. O. Andreae and D. Rosenfeld. Aerosol–cloud–precipitation interactions. part 1. the nature and sources of cloud-active aerosols. *Earth Sci. Rev.*, 89(1):13–41, 2008. 1.1.1

[34] Erika Sasser. *Report to Congress on Black Carbon*. US Environmental Protection Agency, Office of Air Quality Planning and Standards, 2011. 1.1.1

[35] O. V. Kalashnikova, F. P. Mills, A. Eldering, D. Anderson, and R. Mitchell. The effects of smoke and dust aerosols on UV-B radiation in Australia from ground-based and satellite measurements. In *Optics & Photonics*, pages 58860R–58860R. International Society for Optics and Photonics, 2005. 1.1.1

[36] BBC. Evacuation as Calbuco volcano erupts in Chile. `http://www.bbc.com/news/world-latin-america-32425370`, 2015. (document), 1.3

[37] Y. J. Kaufman, D. Tanré, and O. Boucher. A satellite view of aerosols in the climate system. *Nature*, 419:215–223, 2002. 1.1.1, 1.1.2

[38] H. F Graf, B. Langmann, and J. Feichter. The contribution of earth degassing to the atmospheric sulfur budget. *Chem.l Geol.*, 147:131–145, 1998. 1.1.1

[39] D. S. Stevenson, C. E. Johnson, W. J. Collins, and R. G. Derwent. The tropospheric sulphur cycle and the role of volcanic so2. *Geol. Soc. Spec. Pub.*, 213: 295–305, 2003. 1.1.1

[40] Nature. Nature reports Climate Change. `http://www.nature.com/climate/2009/0910/pdf/climate.2009.100.pdf`, 2009. (document), 1.4

[41] P. Forster, V. Ramaswamy, P. Artaxo, T. Berntsen, R. Betts, D. W. Fahey, J. Haywood, J. Lean, D. C. Lowe, G. Myhre, et al. Changes in atmospheric constituents and in radiative forcing. Chapter 2. In *Climate Change 2007. The Physical Science Basis*. 2007. 1.1.2

[42] S. A. Twomey, M. Piepgrass, and T. L. Wolfe. An assessment of the impact of pollution on global cloud albedo. *Tellus Ser. B*, 36:356–366, 1984. 1.1.2

[43] Y. J. Kaufman, I. Koren, L. A. Remer, D. Rosenfeld, and Y. Rudich. The effect of smoke, dust, and pollution aerosol on shallow cloud development over the atlantic ocean. *Proc. Natl. Acad. Sci. U.S.A.*, 102:11207–11212, 2005. 1.1.2

[44] M. O. Andreae, D. Rosenfeld, P. Artaxo, A. A. Costa, G. P. Frank, K. M. Longo, and M. A. F. Silva-Dias. Smoking rain clouds over the amazon. *Science*, 303: 1337–1342, 2004.

[45] Q. Zhang, J. Quan, X. Tie, M. Huang, and X. Ma. Impact of aerosol particles on cloud formation: Aircraft measurements in china. *Atmos. Environ.*, 45:665–672, 2011. 1.1.2

[46] D. M. Murphy and T. Koop. Review of the vapour pressures of ice and supercooled water for atmospheric applications. *Q. J. R. Meteorol. Soc*, 131:1539–1565, 2005. 1.1.2

[47] J. H. Seinfeld and S. N. Pandis. *Atmospheric chemistry and physics: from air pollution to climate change*. John Wiley & Sons, 2012. 1.1.2

[48] T. L. Anderson, R. J. Charlson, S. E. Schwartz, R. Knutti, O. Boucher, H. Rodhe, and J. Heintzenberg. Climate forcing by aerosols – a hazy picture. *Science*, 300: 1103, 2003. 1.1.2

[49] B. Stevens and G. Feingold. Untangling aerosol effects on clouds and precipitation in a buffered system. *Nature*, 461:607–613, 2009. 1.1.2

[50] T. Goren and D. Rosenfeld. Satellite observations of ship emission induced transitions from broken to closed cell marine stratocumulus over large areas. *J. Geophys. Res.*, 117, 2012. 1.1.2

[51] A. S. Ackerman, O. B. Toon, and P. V. Hobbs. Dissipation of marine stratiform clouds and collapse of the marine boundary layer due to the depletion of cloud condensation nuclei by clouds. *Science*, 262:226–229, 1993. 1.1.2

[52] C. Ichoku, R. Levy, Y. J. Kaufman, L. A. Remer, R. R. Li, V. J. Martins, B. N. Holben, N. Abuhassan, I. Slutsker, T. F. Eck, et al. Analysis of the performance characteristics of the five-channel Microtops II Sun photometer for measuring aerosol optical thickness and precipitable water vapor. *J. Geophys. Res.*, 107: AAC–5, 2002. 1.1.3

[53] B. N. Holben, E. Vermote, Y. J. Kaufman, D. Tanre, and V. Kalb. Aerosol retrieval over land from AVHRR data-application for atmospheric correction. *IEEE Trans. Geosci. Remote Sens.*, 30:212–222, 1992. 1.1.3

[54] L. G. Istomina, W. von Hoyningen-Huene, A. A. Kokhanovsky, E. Schultz, and J. P. Burrows. Remote sensing of aerosols over snow using infrared AATSR observations. *Atmos. Meas. Tech. Discuss.*, 4:33–71, 2011. 1.1.3

[55] B. N. Holben, T. F. Eck, I. Slutsker, D. Tanre, J. P. Buis, A. Setzer, E. Vermote, J. A. Reagan, Y. J. Kaufman, T. Nakajima, et al. AERONETA federated instrument network and data archive for aerosol characterization. *Remote Sens. Environ.*, 66:1–16, 1998. 1.1.3, 2.2.2

[56] E. M. Rollin. An introduction to the use of sun-photometry for the atmospheric correction of airborne sensor data. activities of the NERC EPFS in support of the NERC ARSF. In *ARSF Annual Meeting, Keyworth, Nottingham, UK, 22pp*, 2000. 1.1.3

[57] Y. Matsumura and H. N. Ananthaswamy. Toxic effects of ultraviolet radiation on the skin. *Toxicol. Appl. Pharmacol.*, 195:298–308, 2004. 1.2.1, 1.2.2

[58] A. Juzeniene, P. Brekke, A. Dahlback, S. Andersson-Engels, J. Reichrath, K. Moan, M. F. Holick, W. B. Grant, and J. Moan. Solar radiation and human health. *Rep. Prog. Phys.*, 74:066701, 2011. 1.2.1, 1.2.1, 1.2.1, 1.2.2

[59] W. H. O. World Health Organization, I C N I R P. International Commission on Non-Ionizing Radiation Protection, WMO World Meteorological Organization, and UNEP. United Nations Environment Programme. Global solar UV index: A practical guide. 2002. 1.2.1, 1.2.2

[60] Gary E Thomas and Knut Stamnes. *Radiative transfer in the atmosphere and ocean*. Cambridge University Press, 2002. 1.2.1, 1.2.1, 1.2.1, 3.1, 3.2, 3.2, 3.2, 3.3, 3.3, 3.3, 3.3.3, 3.3.4, 3.3.5, 3.3.5, 3.3.5

[61] R. Kozlowski. *Handbook of natural fibres: Processing and applications*, volume 2. Elsevier, 2012. 1.2.1

[62] NASA Goddard Space Flight Center. Ultraviolet Radiation: How it Affects Life on Earth. http://earthobservatory.nasa.gov/Features/UVB/uvb_radiation.php, 2001. (document), 1.6

[63] A. F. McKinlay and B. L. Diffey. "A reference action spectrum for ultraviolet induced erythema in human skin," in Human Exposure to Ultraviolet Radiation: Risks and Regulations, eds. W. R. Passchler and B. F. M. Bosnajakovic. *Elsevier, Amsterdam*, pages 83–87, 1987. (document), 1.2.2, 1.7, 1.2.2

[64] S. Madronich, R. L. McKenzie, L. O. Björn, and M. M. Caldwell. Changes in biologically active ultraviolet radiation reaching the Earth's surface. *J. Photochem. Photobiol., B.*, 46:5–19, 1998. 1.2.2

[65] R. L. McKenzie, L. O. Björn, A. Bais, and M. Ilyasd. Changes in biologically active ultraviolet radiation reaching the Earth's surface. *Photochem. Photobiol. Sci.*, 2:5–15, 2003. 1.2.2

[66] The Royal Netherlands Meteorological Institute and the European Space Egency. Erythemal UV index of 2002 yearly average, maximum and minimum. http://www.temis.nl/uvradiation/GOME/uvyear.php?fb=uviec&Year=2002, 2008. (document), 1.8

[67] NASA Goddard Space Flight Center. Aura: A mission dedicated to the health of Earth's atmosphere. http://earthobservatory.nasa.gov/Features/Aura/Aura_2.php. (document), 1.2.3, 1.2.3, 1.9

[68] S. Chapman. On ozone and atomic oxygen in the upper atmosphere. *Philos. Mag.*, 10:369–383, 1930. 1.2.3

[69] R. W. Portmann, J. S. Daniel, and A. R. Ravishankara. Stratospheric ozone depletion due to nitrous oxide: influences of other gases. *Phil. Trans. R. Soc. B*, 367: 1256–1264, 2012. 1.2.3

[70] S. O. Andersen, D. Brack, and J. Depledge. A global response to HFCs through fair and effective ozone and climate policies. *The Royal Institute for International Affairs (Chatham House), July*, 2014. 1.2.3

[71] NASA Goddard Space Flight Center. What is the Ozone Hole? http://ozonewatch.gsfc.nasa.gov/facts/hole_SH.html, 2013. 1.2.3, 1.2.3

[72]

[73] Encyclopedia Britannica. Atmosphere. http://global.britannica.com/science/atmosphere/Cloud-processes, 2013. 1.3

[74] C. N. Hewitt and A. V. Jackson. *Handbook of atmospheric science: Principles and applications*. John Wiley & Sons, 2008. 1.3

[75] Arne Dahlback. Measurements of biologically effective UV doses, total ozone abundances, and cloud effects with multichannel, moderate bandwidth filter instruments. *Appl. Opt.*, 35:6514–6521, 1996. 1.3.1

[76] P. Kulkarni, P. A. Baron, and K. Willeke. *Aerosol measurement: Principles, Techniques, and Applications*. John Wiley & Sons, 2011. 1.3.2

[77] British Broadcasting Corporation (BBC). The solar system. http://www.bbc.co.uk/education/guides/zk8hvcw/revision/2, 2015. (document), 1.11

[78] K. H. Lee, Z. Li, Y. J. Kim, and A. Kokhanovsky. Atmospheric aerosol monitoring from satellite observations: a history of three decades. In *Atmospheric and biological environmental monitoring*, pages 13–38. Springer, 2009. 1.3.2

[79] European Space Agency (ESA). SCIAMACHY Product Handbook. https://earth.esa.int/web/guest/missions/esa-operational-eo-missions/envisat/instruments/sciamachy-handbook/wiki/-/wiki/SCIAMACHY%20Handbook/Instrument+Operations, 2015. (document), 1.12

[80] B. A. K. Høiskar, R. Haugen, T. Danielsen, A. Kylling, K. Edvardsen, A. Dahlback, B. Johnsen, M. Blumthaler, and J. Schreder. Multichannel moderate-bandwidth filter instrument for measurement of the ozone-column amount, cloud transmittance, and ultraviolet dose rates. *Appl. Opt.*, 42:3472–3479, 2003. 2.1

[81] France CIMEL Electronique, Paris. Multiband photometer CE318. http://support.cimel.fr/photo/pdf/man_ce318_us.pdf, 2015. 2.2.1, 2.2.2

[82] B. N. Holben, A. Smirnov, T. F. Eck, I. Slutsker, N. Abuhassan, W. W. Newcomb, J. S. Schafer, D. Tanre, B. Chatenet, and F. Lavenu. An emerging ground-based aerosol climatology- aerosol optical depth from AERONET. *J. Geophys. Res.*, 106:12067–12097, 2001. 2.2.2

[83] R. D. McPeters, P. K. Bhartia, A. J. Krueger, J. R. Herman, B. M. Schlesinger, C. G. Wellemeyer, C. J. Seftor, G. Jaross, S. L. Taylor, T. Swissler, S. L. Taylor, O. Torres, and C. G. Wellemeyer. Nimbus-7 Total Ozone Mapping Spectrometer (TOMS) data products user's guide. 1384, 1996. 2.3.1

[84] R. D. McPeters, P. K. Bhartia, A. J. Krueger, J. R. Herman, C. G. Wellemeyer, C. J. Seftor, G. Jaross, O. Torres, L. Moy, G. Labow, W. Byerl, S. L. Taylor, T. Swissler, and R. P. Cebula. Earth probe total ozone mapping spectrometer (TOMS): Data products user's guide. 1998. 2.3.1, 2.3.2

[85] P. F. Levelt, E. Hilsenrath, G. W. Leppelmeier, G. H. J. Van den Oord, P. K. Bhartia, J. Tamminen, J. F. De Haan, and J. P. Veefkind. Science objectives of the Ozone Monitoring Instrument. *(IEEE) Trans. Geosci. Remote Sens.*, 44:1199–1208, 2006. 2.3.3, 2.3.3

[86] O. Torres, A. Tanskanen, B. Veihelmann, C. Ahn, R. Braak, P. K. Bhartia, P. Veefkind, and P. Levelt. Aerosols and surface UV products from Ozone Monitoring Instrument observations: An overview. *J. Geophys. Res.*, 112, 2007. 2.3.3, 2.3.3

[87] M. R. Schoeberl, A. R. Douglass, E. Hilsenrath, P. K. Bhartia, R. Beer, J. W. Waters, M. R. Gunson, L. Froidevaux, J. C. Gille, Levelt P. F. Barnett, J. J., and P. DeCola. Overview of the EOS Aura mission. *IEEE Trans. Geosci. Remote Sens.*, 44:1066–1074, 2006. (document), 2.3.3, 2.4, 2.3.3

[88] A. Tanskanen, N. A. Krotkov, J. R. Herman, and A. Arola. Surface ultraviolet irradiance from OMI. *(IEEE) Trans. Geosci. Remote Sens.*, 44:1267–1271, 2006. 2.3.3

[89] D. T. Shindell, D. Rind, and P. Lonergan. Increased polar stratospheric ozone losses and delayed eventual recovery owing to increasing greenhouse-gas concentrations. *Nature*, 392:589–592, 1998. 2.3.3

[90] A. Tanskanen. Lambertian surface albedo climatology at 360 nm from TOMS data using moving time-window technique. In *Proceedings of the XX quadrennial ozone symposium*, volume 1, 2004. 2.3.3

[91] P. Weihs, M. Blumthaler, H. E. Rieder, A. Kreuter, S. Simic, W. Laube, A. W. Schmalwieser, J. E. Wagner, and A. Tanskanen. Measurements of UV irradiance within the area of one satellite pixel. *Atmos. Chem. Phys.*, 8:5615–5626, 2008. 2.3.3

[92] B. Hamre, S. Stamnes, J. J. Stamnes, and K. Stamnes. AccuRT: A Versatile Tool for Radiative Transfer in Coupled Media like Atmosphere-Ocean Systems. In *Ocean Optics XXII*, Portland, ME, USA, Oct. 2014. URL `http://www.geminor.com/media/Hamre_OO2014_AO_portrait_v3.pdf`. 3.1

[93] K. Stamnes and J. J. Stamnes. *Radiative Transfer in Coupled Environmental Systems: An Introduction to Forward and Inverse Modeling*. John Wiley & Sons, 2015. 3.1

[94] Curtis D Mobley. *Light and water: Radiative transfer in natural waters*. Academic press, San Diego, CA, 1994. 3.1

[95] NASA Goddard Space Flight Center. The Electromagnetic Spectrum. `http://imagine.gsfc.nasa.gov/science/toolbox/emspectrum1.html`, 2013. 3.2

[96] MrEclipse.com. Total Lunar Eclipse of 2014 April 15 - Mid-Totality. `http://www.mreclipse.com/LEphoto/TLE2014Apr/TLE2014Apr-1182.html`, 2014. (document), 3.1

[97] L. G. Henyey and J. L. Greenstein. Diffuse radiation in the galaxy. *Astrophys. J.*, 93:70–83, 1941. 3.2

[98] L. Rayleigh. A re-examination of the light scattered by gases in respect of polarisation. i. experiments on the common gases. *Proc. Roy. Soc.*, 97:435–450, 1920. 3.2